



# 1 Near-real time detection of unexpected atmospheric events using 2 Principal Component Analysis on the IASI radiances

3 Adrien Vu Van<sup>1,2</sup>, Anne Boynard<sup>1,2</sup>, Pascal Prunet<sup>2</sup>, Dominique Jolivet<sup>3</sup>, Olivier Lezeaux<sup>2</sup>, Patrice  
4 Henry<sup>4</sup>, Claude Camy-Peyret<sup>5</sup>, Lieven Clarisse<sup>6</sup>, Bruno Franco<sup>6</sup>, Pierre Coheur<sup>6</sup> and Cathy  
5 Clerbaux<sup>1,6</sup>

6 <sup>1</sup>LATMOS/IPSL, Sorbonne Université, UVSQ, CNRS, Paris, 75005, France

7 <sup>2</sup>SPASCIA, Ramonville-Saint-Agne, 31520, France

8 <sup>3</sup>HYGEOS, Lille, 59000, France

9 <sup>4</sup>CNES (Centre National d'Etudes Spatiales), Toulouse, 31400, France

10 <sup>5</sup>IPSL, Institut Pierre-Simon Laplace, Paris, 75005, France

11 <sup>6</sup>Université libre de Bruxelles (ULB), Spectroscopy, Quantum Chemistry and Atmospheric Remote Sensing  
12 (SQUARES), Bruxelles, 1050, Belgium

13 *Correspondence to:* Anne Boynard (anne.boynard@latmos.ipsl.fr)

14 **Abstract.** The three IASI instruments on-board the Metop family of satellites have been sounding the atmospheric  
15 composition since 2006. More than 30 atmospheric gases can be measured from the IASI radiance spectra, allowing  
16 the improvement of weather forecasting, and the monitoring of atmospheric chemistry and climate variables.

17 The early detection of extreme events such as fires, pollution episodes, volcanic eruptions, or industrial releases is key  
18 to take safety measures to protect inhabitants and the environment in the impacted areas. With its near real time  
19 observations and good horizontal coverage, IASI can contribute to the series of monitoring systems for the systematic  
20 and continuous detection of exceptional atmospheric events, in order to support operational decisions.

21 In this paper, we describe a new approach for the near real time detection and characterization of unexpected events,  
22 which relies on the principal component analysis (PCA) of IASI radiance spectra. By analysing both the IASI raw and  
23 compressed spectra, we applied a PCA-granule based method on various past well documented extreme events such  
24 as volcanic eruptions, fires, anthropogenic pollutions and industrial accidents. We demonstrate that the method is well  
25 suited to detect spectral signatures for reactive and weak absorbing gases, even for sporadic events. Long-term records  
26 are also generated for fire and volcanic events, by analysing the available IASI/Metop-B data record.

## 27 1 Introduction

28 Atmospheric composition is changing fast locally, under natural and anthropogenic influences combined. Fire activity  
29 and local urban pollution are likely to increase in a warming climate (Hart, 2022). With their potential consequences  
30 on society and health, monitoring the events that impact atmospheric composition becomes more and more important.

31 Since the end of 2006 the IASI mission has been probing the troposphere from satellite to monitor the atmospheric  
32 composition globally, onboard of 3 successive Metop satellites (Clerbaux et al., 2009). Observation records and trends  
33 are available for several infrared absorbing species, such as methane (CH<sub>4</sub>) (García et al., 2018), carbon monoxide  
34 (CO) (George et al., 2009), ammonia (NH<sub>3</sub>) (Van Damme et al., 2021), ozone (O<sub>3</sub>) (Dufour et al., 2018; Wespes et al.,  
35 2019) and dust (Capelle et al., 2014; Clarisse et al., 2019). As the first goal of this mission is to feed meteorological



36 forecast using data assimilation, radiance Level 1C (LIC) data are received in near real time, around 2-3 hours after  
37 the overpass of the satellite. This makes the detection of exceptional events possible, potentially right after they occur,  
38 such as large biomass burning fires (Turquety et al., 2009; R'Honi et al., 2013), anthropogenic pollution episodes  
39 (Boynard et al., 2014) or volcanic eruptions (Wright et al., 2022). With more than 1.2 million of radiance spectra per  
40 instrument per day, the search for local extreme events in near real time is not straightforward. A limitation is also  
41 associated with the lack of data when clouds are present in the field of view, as the retrieval algorithms fail to properly  
42 derive atmospheric concentrations for trace gases. Cloudy data are hence filtered.

43 Soon after the launch of the first IASI instrument, it has been suggested to use the principal component analysis (PCA)  
44 method to reduce data volumes by reconstructing the radiances using only the leading eigenvectors (Matricardi, 2010).  
45 This compression not only allows to heavily decrease the data volume but also to ease the data dissemination. Now  
46 available through the EUMETSAT (European organization for the exploitation of METeorological SATellites)  
47 Advanced Retransmission Service (EARS-IASI), the PCA method allows meteorological centers to directly assimilate  
48 the principal components (Collard et al., 2010; Matricardi et al., 2014; Guedj et al., 2015). It was also demonstrated  
49 that using reconstructed IASI radiance results in a substantial reduction of random instrument noise for the analysis of  
50 trace gases such as  $\text{NH}_3$  or sulfur dioxide ( $\text{SO}_2$ ) (Atkinson et al., 2010). However, it was decided to continue the  
51 distribution of the entire radiance spectra (8461 spectral channels) as one of the concerns in the use of the PCA method,  
52 for atmospheric chemistry studies, was the detection of spectral features associated with minor trace gases linked with  
53 rare events in the reconstructed spectra. Examples are volcanic eruptions, which all differ in terms of gas and type of  
54 ash emitted, and hence not enough representative cases were available in the training set. The same holds for biomass  
55 burning fires releasing different amounts of specific species depending on the type of vegetation burned. With the  
56 advent of the second and third IASI instrument together with the improvement of retrieval algorithms over time, a  
57 number of short- and long-lived trace gases were identified in the IASI spectra above or downwind from strong  
58 emission sources (Clarisse et al., 2011; De Longueville et al., 2021).

59 This paper describes the potential of the PCA applied on the IASI LIC (apodized radiance) data for the automatic,  
60 near real time detection and characterization of exceptional events. The paper is organized as follows: Section 2  
61 describes the IASI instrument and the dataset used in this study. Section 3 describes the PCA method. In Section 4, an  
62 innovative approach based on the PCA method and IASI data granules is presented, which allows spectral  
63 characterization of species in near real time. In Section 5, different case studies of exceptional past events are discussed,  
64 such as volcanic, fire, and anthropogenic pollution episodes, along with industrial accidents, detected by IASI/Metop-  
65 A and -B. Finally, conclusions are given in Section 6.

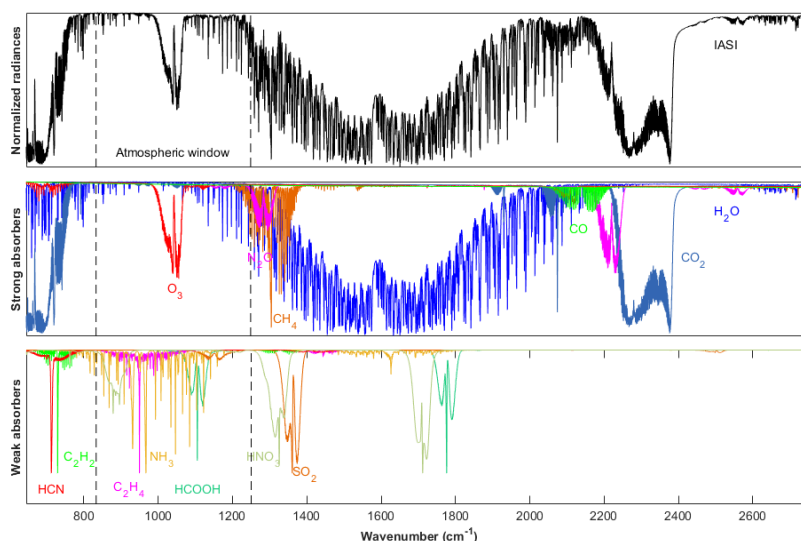
## 66 **2 The IASI radiance data**

67 IASI is a Fourier transform infrared spectrometer, which records the thermal infrared (TIR) radiation emitted by the  
68 Earth and the atmosphere, between  $645 \text{ cm}^{-1}$  and  $2760 \text{ cm}^{-1}$ , with 8461 channels sampled every  $0.25 \text{ cm}^{-1}$  and a spectral  
69 resolution of  $0.5 \text{ cm}^{-1}$ . An example of IASI spectrum along with the absorption band of several species is illustrated in  
70 Fig. 1. Table A1 in Appendix A provides the selected spectral ranges defined for this work. Bands are identified with  
71 HITRAN spectroscopic absorption parameters (Gordon et al., 2017, 2022) for infrared absorbing molecules. In this



72 work IASI-A and IASI-B are used as a similar dataset. The IASI-A dataset is used for the study of events before the  
73 launch of IASI-B and for creating the PCA training database (described here-after), and the IASI-B complete dataset  
74 is used for data after 2013 to present. The two datasets have been shown to be highly consistent with no significant  
75 drifts over time (García et al., 2016).

76 Each IASI instrument provides more of 1.2 million of spectra per day. IASIL1C data are disseminated by EUMETSAT  
77 in 3-minute files (called “granule” hereafter) less than 3 hours after each overpass. Each granule contains 22 or 23  
78 IASI scan lines with 120 pixels per line. With a wide swath width of ~2200 km, global observations are provided twice  
79 a day, at 9:30 AM and 9:30 PM local time. IASI has an instantaneous field of view (FOV) at nadir with a spatial  
80 resolution of 50 km x 50 km, composed of 2 x 2 circular pixels (IFOV), each corresponding to a 12 km diameter  
81 footprint on the ground at nadir (Clerbaux et al. 2009).



82

83 **Figure 1: Top panel: Example of IASI spectrum. Middle and bottom panels: radiative transfer simulations for the main and**  
84 **weaker infrared absorbers, respectively.**

85 The atmospheric concentrations of some species are routinely retrieved from the spectral signatures (George et al.,  
86 2009; Clarisse et al., 2011; Van Damme et al., 2013) and distributed through the AERIS database (iasi.aeris-data.fr).  
87 Some exceptional events have been studied in details such as the 2010 Russian fires (R’honi et al., 2013), pollution in  
88 the North China Plain (Boynard et al., 2014), and SO<sub>2</sub> anthropogenic pollution (Bauduin et al., 2014, 2016).

### 89 **3 The Principal Component Analysis Method**

#### 90 **3.1 Basic concepts**

91 The PCA method for high spectral resolution sounders, such as IASI, is described in Atkinson et al. (2008). This  
92 method is well suited to efficiently represent the limited amount of information contained in the 8641 IASI channels.



93 It relies on the use of a dataset of thousands of spectra representing the full range of atmospheric conditions from which  
94 the principal components are calculated, the so-called “training database”.

95 Let  $\mathbf{Y}$  be a  $m \times n$  matrix representing a set of radiance spectra (where  $m$  is the number of channels and  $n$  is the number  
96 of observations) and  $\bar{y}$  its mean, the covariance matrix,  $S_\epsilon$  ( $m \times m$ ) of the noise-normalized spectra is given by:

$$97 \quad S_\epsilon = \frac{1}{n} \sum_{i=1}^n y_i N^{-1} y_i^T - \bar{y} N^{-1} \bar{y}^T \quad (1)$$

98 where  $N$  ( $m \times m$ ) is the instrument noise covariance matrix. The PCA is based on the eigen decomposition of the  
99 matrix  $S_\epsilon$ :

$$100 \quad S_\epsilon = E \lambda E^T \quad (2)$$

101 where  $\mathbf{E}$  is the matrix  $m \times m$  of eigenvectors and  $\lambda$  their associated eigenvalues.

102 The projection of a measured spectrum  $y$  in the eigenspace  $E$  is computed from:

$$103 \quad p = E^T N^{-1} (y - \bar{y}) \quad (3)$$

104  $p$  (dimension  $m$ ) is the vector of the principal component scores, and is the representation of  $y$  in the eigenspace.  
105 Because most of the atmospheric signal is contained in a relatively small number of leading eigenvectors, with the  
106 higher-rank eigenvectors containing mainly instrument noise, it is possible to discard the higher-rank eigenvectors,  
107 and conservatively represent the spectrum in the eigenspace by a truncated vector of principal component scores,  $p^*$   
108 of rank  $m^*$  ( $m^* < m$ ).  $p^*$  is thus a compressed representation of  $y$ . The reconstructed spectrum,  $\tilde{y}$  (dimension  $m$ ) is  
109 given by:

$$110 \quad \tilde{y} = \bar{y} + N E^* p^* \quad (4)$$

111 where  $E^*$  is the matrix of the  $m^*$  first eigenvectors or principal components. We define the normalized residual vector  
112  $r$  (dimension  $m$ ) of the reconstruction by:

$$113 \quad r = N^{-1} (y - \tilde{y}) \quad (5)$$

114 By definition, if  $m^*$  is taken equal to  $m$ ,  $\tilde{y} = y$  and the residual is the null vector. In nominal cases if the truncation  
115 rank is carefully chosen,  $r$  essentially contains noise. Several techniques exist to estimate  $m^*$  the optimal number of  
116 principal components in order to keep the essential part of the atmospheric signal and to remove the eigenvectors  
117 containing mainly the measurement noise (e.g., Antonelli et al., (2004), Atkinson et al., (2010)).

### 118 **3.2 Construction of the training database**

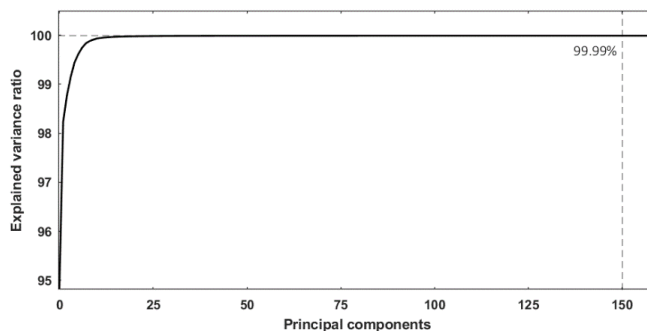
119 For this study, around 120 000 IASI/Metop-A LIC spectra were selected during a full year (which was chosen as a  
120 nominal year for avoiding excessive occurrence of extreme events such fires and volcanoes) on the global scale. The  
121 database contains spectra associated with a good quality flag in order to only keep reliable data, acquired indifferently  
122 during the day and the night, over land and sea, and regardless of the cloud cover. For each month of the year 2013



123 spectra were selected every five days (1, 6, 11, 16, 21 and 26 of each month). In order to not over-represent high  
124 latitudes (due to the frequent overpasses over this area because of the polar orbiting), the following method was applied:  
125 - between 90 and 75° only one spectrum is selected  
126 - between 75 and 60°, two spectra are selected  
127 - between 60 and 45°, three spectra are selected  
128 - between 45 and 30°, four spectra are selected  
129 - between 30 and 15°, five spectra are selected  
130 - between 15 and 0°, six spectra are selected  
131 Then a random selection was also applied to represent all the conditions of acquisition in terms of IASI scan lines and  
132 IFOV.

### 133 3.3 Number of eigenvectors, reconstruction score and “indicators”

134 The eigen values quantify the explained variability of eigen vectors. These values are sorted in descending order. The  
135 minimum number of eigenvectors needed to reproduce the signal in the raw radiances can be determined by analyzing  
136 the magnitude of the eigenvalues. As shown in Fig. 2, around 20 principal components allow to depict most of the  
137 atmospheric variability. However, as shown in Goldberg et al. (2003), keeping more than the first principal components  
138 avoids a loss of information in the reconstructed spectra. In this study it is proposed to study the 3 IASI bands together  
139 and choose the first 150 eigenvectors (over 8461) (Atkinson, 2010) to explain 99.99% of the atmospheric variability,  
140 which allows to reduce the random noise without losing information in most of the reconstructed spectra.



141  
142 **Figure 2: Evolution of the explained variance ratio in function of the rank of principal components. 99.99% of the**  
143 **atmospheric variability is depicted by the 150 first eigenvectors.**

### 144 4 The IASI-PCA granule-extrema (GE) based method

145 In order to use the maximum of information contained in the spectra for the different absorbing molecules, an original  
146 method exploiting the full IASI spectral residual is developed. This approach, based on the IASI-PCA method, focuses



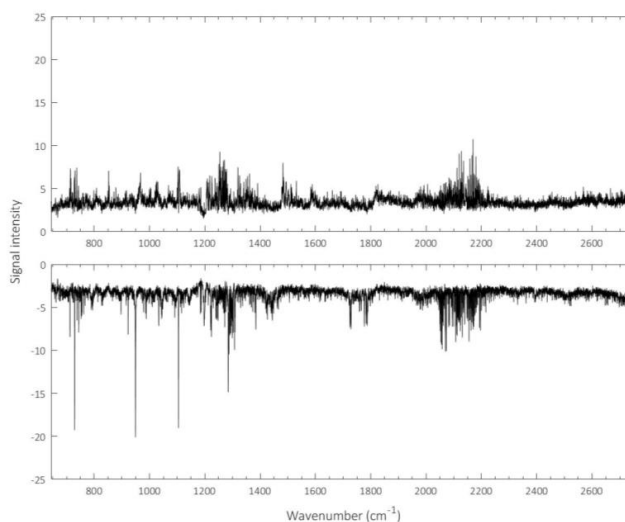
147 on intense spectral lines or narrow absorption bands of  $0.5 \text{ cm}^{-1} - 2.0 \text{ cm}^{-1}$  width, depending on the molecular  
148 absorption peaks (see Table A1 in Appendix A).

#### 149 **4.1 Granule maxima and minima**

150 The near real time detection of exceptional events is performed on the IASI granule. The choice of applying the method  
151 on the granule is convenient for the near real time aspect as it represents 3 minutes of IASI data which are received  
152 every few 1-2 hours by the antenna. It allows not only a fast computing and statistical approach above a given  
153 geographical region but also a preliminary approach allowing to characterize and localize outliers.

154 Each granule contains  $\sim 2700$  radiance spectra, from which we compute the corresponding residuals. Indicators based  
155 on the residuals statistics over the granule are calculated, such as minima, maxima, means, median and standard  
156 deviations for each spectral channel. For a given granule, the largest positive and negative residual value for each  
157 spectral channel is recorded in two arrays, called in the following “Granule Maxima” (GMA) and “Granule Minima”  
158 (GMI) pseudo spectra. GMA and GMI pseudo spectra are associated with reconstruction errors of spectral emission  
159 lines and absorption lines, respectively. The spectral vectors containing the mean of the spectral residuals (denoted  $m$   
160 in the following) and the standard deviation of the spectral residuals (denoted  $\sigma$  in the following) over the granule are  
161 also recorded.

162 **Figure 3 illustrates an example of GMA and GMI pseudo spectra for an intense fire event that occurred in Australia on 1**  
163 **January 2020. The GMI pseudo spectrum (bottom panel) is characterized by detectable spectral features associated with a**  
164 **poor reconstruction around 700, 950, 1100 or 2100  $\text{cm}^{-1}$ . Using spectroscopic database allows to associate some of these**  
165 **strong peaks with contribution of different atmospheric components (see Section 5 for the identification of the molecules).**  
166 **Similar spectral features can be seen in the GMA pseudo spectrum (top panel) albeit in emission and less intense.**



167

168 **Figure 3: Granule Maxima (GMA) (top) and Granule Minima (GMI) (bottom) pseudo spectra obtained from a granule of**  
169 **IASI/Metop-B L1C data on 1 January 2020 over Australia.**

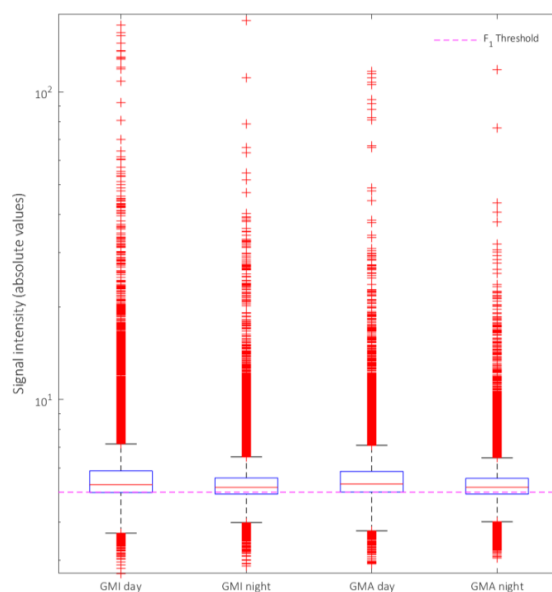


170 **4.2 Detection thresholds**

171 The identification of absorbing species is done using their spectroscopic properties. These parameters are provided  
172 from the HITRAN spectroscopic parameter database or in the literature if not available (see Table A1 in Appendix A).  
173 However, in order to apply the IASI-PCA-GE method for the systematic analysis of data of interest on the Metop-B  
174 time series, statistical thresholds are defined. Three different thresholds were defined, as described hereafter.

175 A dataset of 43 000 granules is created from random selection of granules taken on 1<sup>st</sup> day of each month between  
176 April 2013 and April 2021, containing both outlier and regular spectra during the Metop-B time series. Figure 4 shows  
177 the statistical distribution of the spectral extrema (in absolute values) calculated in the GMI and GMA pseudo spectra  
178 for 21 500 granules for both daytime and nighttime conditions. The blue box represents the 25<sup>th</sup> percentile, the median  
179 and the 75<sup>th</sup> percentile in the data. The upper and lower adjacent values are in black, and the red crosses respectively  
180 higher or lower than those values are considered as “outliers” in the dataset.

181 An absolute signal intensity for the 25<sup>th</sup> percentile is found around 5 (magenta dashed line) for all conditions. As a low  
182 filtering effect is expected from this threshold, in order to mitigate false negative detection even in case of low intensity  
183 events, the threshold  $F_1 = 5$  is defined on the 25<sup>th</sup> percentile. Then, the extremum of each granule will be compared to  
184  $F_1$  to be selected or rejected by the algorithm.



185

186 **Figure 4: Distribution of normalized GMI and GMA extrema in absolute values calculated from 21 500 granules both for**  
187 **day- and night-time conditions. The 25th percentile, the median and the 75th percentile are respectively represented at the**  
188 **bottom, middle and top of the blue box. The magenta dashed line also representing the 25th percentile of the signal intensity**  
189 **is around 5 for both conditions. The upper (top) and lower (bottom) adjacent values are represented in black.**



190 For a given granule selected using  $F_1$ , a second threshold  $F_2$  is applied to select the channels associated with a poor  
191 reconstruction in the GMI or GMA (depending on the atmospheric conditions). This threshold depends on the mean  
192 and standard deviation spectral vectors,  $m$  and  $\sigma$  respectively, calculated over the granule. All IASI channels  
193 characterized by a value (in absolute) larger than  $F_2 = \text{abs}(m) + 1 * \sigma$  are selected.

194 Finally, a third threshold  $F_3$  is empirically defined to reduce the noise without losing information. These thresholds are  
195 defined based on the 21 500 GMI and 21 500 GMA pseudo spectra dataset previously introduced. The 99<sup>th</sup> percentile  
196 value computed for each specific channel associated with a strong absorption of a molecule is selected as a  $F_3$  threshold.  
197 Table 1 provides the signal intensity thresholds for several species for daytime and nighttime conditions.

198 **Table 1: Signal intensity thresholds ( $F_3$ ) for several species for day- and night-time conditions defined to reduce the noise**  
199 **in GMA or GMI results.**

Molecule	Channel (cm <sup>-1</sup> )	GMI day	GMI night	GMA day	GMA night
H <sub>2</sub> O	712.50	-4.42	-4.41	4.10	4.06
C <sub>2</sub> H <sub>2</sub>	729.25	-4.01	-3.92	3.94	3.88
C <sub>4</sub> H <sub>4</sub> O	744	-4.13	-4.10	3.77	3.76
HONO	790	-4.09	-4.08	4.18	4.06
NH <sub>3</sub>	967	-8.01	-4.60	4.46	4.70
C <sub>2</sub> H <sub>4</sub>	949	-4.41	-4.39	4.29	4.25
CH <sub>3</sub> OH	1034	-4.35	-4.27	4.40	4.30
HCOOH	1105	-6.06	-4.69	4.47	4.26
HNO <sub>3</sub>	1326	-6.93	-6.43	6.01	6.38
SO <sub>2</sub>	1345	-7.52	-4.92	4.38	4.46
CO	2111	-6.89	-4.72	4.58	4.28

200

### 201 4.3 Towards a detection of extreme events in near real time

202 Right after the reception of each IASI 3-minutes granule, the two GMA/GMI pseudo spectra are calculated as well as  
203 other statistics of the residual over the granule. Then the three different thresholds defined in Section 4.2 are applied  
204 to the GMA/GMI pseudo spectra in order to localize the pixels potentially associated with an event and the associated  
205 channels. In case of anomalies (i.e., threshold overrun) in the GMA/GMI pseudo spectra, an alert is set-up along with  
206 the targeted channels identified. the corresponding absorbing species are identified by associating the targeted channels  
207 with their spectral range (see Appendix A), and the spatial distribution mapping of the detected pixels in the 3-minute  
208 granule is produced. This allows to visualize and further study exceptional events. The IASI-PCA-GE method was  
209 validated for past and documented events, four of which are described hereafter. It is now running continuously,  
210 delivering email alerts on a routine basis using the near real time IASI L1C radiance data. Most of these alerts are  
211 associated with fires and volcanic eruptions.

212





## 213 5 Case studies

214 This section presents a demonstration of the IASI-PCA-GE method for several past extreme events. The method is  
215 applied to IASI/Metop-A and the IASI/Metop-B L1C radiance data. Table 2 gives a brief description of the case studies  
216 presented hereafter.

217 **Table 2: Brief description of the four case studies analyzed in this section.**

Type	Location	Date	AM/PM orbit	Instrument	Observed molecules
<b>Volcanic Eruption</b>	Ubinas/ Peru	20/07/2019	AM	IASI- B	SO <sub>2</sub> , HNO <sub>3</sub>
<b>Fires</b>	Australia	01/01/2020	AM	IASI-B	HCN, C <sub>2</sub> H <sub>2</sub> , C <sub>2</sub> H <sub>4</sub> , HCOOH, CO, NH <sub>3</sub> , C <sub>4</sub> H <sub>4</sub> O, CH <sub>3</sub> OH
<b>Anthropogenic pollution</b>	China	13/01/2013	PM	IASI-A	NH <sub>3</sub> , SO <sub>2</sub> , CO
<b>Industrial accident</b>	Iraq	24/10/2016	PM	IASI-B	SO <sub>2</sub> , HNO <sub>3</sub>

218

219 For each event, we identify the molecules in the outliers through analysis of the residual statistic, in order to identify  
220 the spectroscopic feature characteristic of the studied gas, over a granule and applying the IASI-PCA-GE method. We  
221 also provide distribution maps to illustrate the spatial distribution of the target event. When available, the maps are  
222 compared to the existing retrieved IASI products (NH<sub>3</sub>: Van Damme et al., 2021; CH<sub>3</sub>OH and HCOOH: Franco et al.,  
223 2018; HCN: Rosanka et al., 2021; SO<sub>2</sub>: Clarisse et al., 2012).

### 224 5.1 Volcanic eruption events

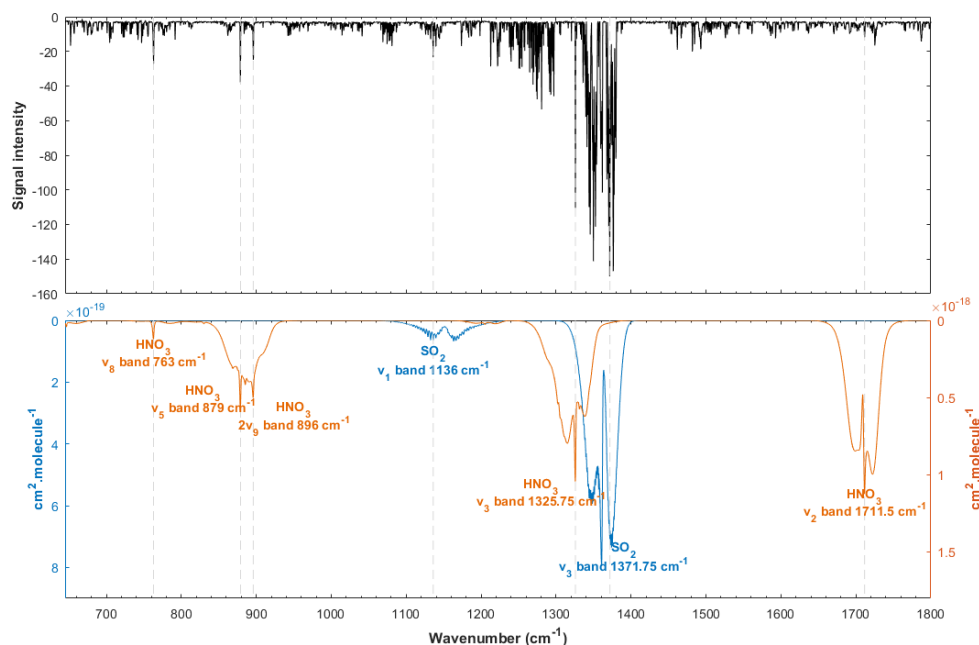
225 Volcanic eruptions have a major impact on atmospheric composition. SO<sub>2</sub>, which has several strong absorption bands  
226 in the TIR spectral range, is the most common molecule observed in the volcanic plume (Clarisse et al., 2012). Several  
227 other species were previously observed by satellites in volcanic eruptions such as hydrochloric acid (HCl) (Clarisse et  
228 al., 2020), hydrogen sulfide (H<sub>2</sub>S) (Clarisse et al., 2011) and sulfuric acid (H<sub>2</sub>SO<sub>4</sub>) (Ackerman et al., 1994; Karagulian  
229 et al., 2010), which can be injected in the stratosphere in case of high-altitude eruption (Rose et al., 2006; Millard et  
230 al., 2006).

#### 231 5.1.1 The Ubinas (Peru) case study

232 The IASI-PCA-GE method was applied to several volcanic eruptions. Here, we illustrate the findings for the eruption  
233 in Ubinas, Peru on 20 July 2019 (Venzke et al., 2019). Instituto Geofísico del Perú (IGP) mentioned that seismic  
234 activity suddenly increased during June 2019 and remained high during July 2019 with important ash emissions  
235 causing the evacuation of the population in some areas affected by ashfall. Figure 5 illustrates the normalized GMI  
236 pseudo spectrum obtained during this volcanic eruption corresponding to a granule taken in the area of the plume  
237 during daytime. A large difference between the reconstructed spectra and raw spectra is located in the SO<sub>2</sub> ν<sub>3</sub> band  
238 around 1371.5 and 1376 cm<sup>-1</sup> which is in agreement with results of Clarisse et al. (2008, 2012) showing the sensitivity



239 of the  $\nu_3$  band. Indeed, the peak found at  $1371.5\text{ cm}^{-1}$  is associated with the presence of  $\text{SO}_2$  plume in the upper  
240 troposphere/lower stratosphere ( $\sim 14\text{ km}$ ,  $150\text{ hPa}$ ) between  $0.5\text{ DU}$  and  $200\text{ DU}$  (saturation) (Clarisse et al., 2011).  
241 Such detection is expected in this case due to the high quantity of  $\text{SO}_2$  emitted. It is worth noting that other peaks in  
242 the GMI pseudo spectrum also show strong absorptions, which were associated with  $\text{HNO}_3$ . Even if this constituent  
243 has previously been reported in volcanic plumes in some active degassing volcanoes (Mather et al., 2004), peaking in  
244 the GMI at  $\sim 763\text{ cm}^{-1}$ ,  $879\text{ cm}^{-1}$  and  $897\text{ cm}^{-1}$ , and  $1325\text{ cm}^{-1}$  associated with  $\nu_8$ ,  $\nu_5$ ,  $2\nu_9$ ,  $\nu_3$  and  $\nu_2$  nitric acid absorption  
245 bands, respectively, it has never been observed by remote sensing before. As the analysis of the IASI  $\text{HNO}_3$  L2 products  
246 shows no  $\text{HNO}_3$  enhancement, further investigations were performed to identify where the signature comes from.



247

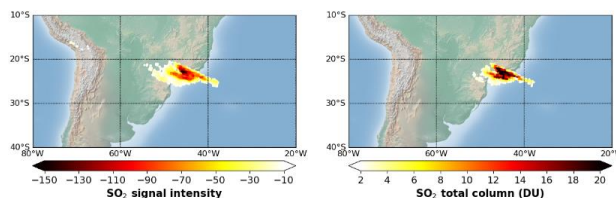
248 **Figure 5: Top: Example of GMI pseudo spectrum calculated from IASI/Metop-B L1C data during a volcanic eruption in**  
249 **Ubinas, Peru on 20 July 2019 in the morning (AM orbit). Bottom: HITRAN spectroscopic parameters associated with the**  
250 **absorption of  $\text{HNO}_3$  and  $\text{SO}_2$  are shown in blue and in orange, respectively.**

251 The  $\text{HNO}_3$  detection by the IASI-PCA-GE method was further investigated by applying the whitening method  
252 proposed by De Longueville et al. (2021). The use of a covariance matrix, calculated from a set of IASI spectra shows  
253 similar results as those found with the IASI- IASI-PCA-GE method. However, using a covariance matrix excluding  
254 the  $\text{SO}_2$  absorption band, no  $\text{HNO}_3$  spectral feature was found. This suggests that no acid nitric is present in the plume.  
255 The features found in the  $\text{HNO}_3$  absorption band by the IASI-PCA-GE method is likely related to  $\text{SO}_2$  features given  
256 that the  $\text{SO}_2$   $\nu_3$  absorption band superimposes with the  $\text{HNO}_3$   $\nu_3$  band.



257 Furthermore, other spectral signatures remain difficult to characterize in the 1200 – 1300 cm<sup>-1</sup> spectral domain. This  
258 spectral range corresponds to the absorption of different volcanic compounds such as ash, aerosols and other possible  
259 volcanic molecules such as H<sub>2</sub>S or H<sub>2</sub>SO<sub>4</sub> (Karagulian et al., 2010) but is also sensible to strong H<sub>2</sub>O absorptions.

260 After applying the thresholds filters defined in Section 4.2 to the GMI pseudo spectrum, the spatial distribution of the  
261 pixels associated with outliers can be mapped. Figure 6 shows a plume of SO<sub>2</sub> (left) in Southeast America, with large  
262 signal intensity values reaching around -150 in the center of the plume. The spatial distribution of the retrieved IASI  
263 SO<sub>2</sub> L2 operational products (right) also shows the plume located in Southeast America and is in excellent agreement  
264 with the SO<sub>2</sub> plume detected from the IASI-PCA-GE method.

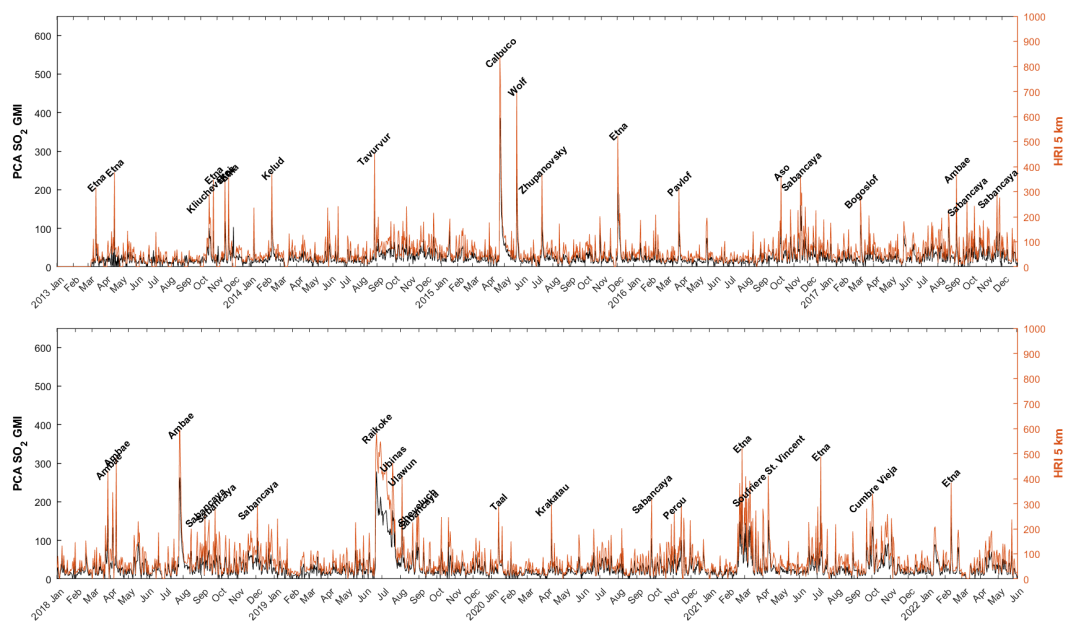


265

266 **Figure 6: Left: Spatial distribution of the residual values associated with SO<sub>2</sub> IASI-PCA-GE detections, using IASI/Metop-**  
267 **B radiance data recorded on 20 July August 2019 in the morning (AM orbit). Right: SO<sub>2</sub> total column retrievals in Dobson**  
268 **Units.**

### 269 5.1.2 Volcanic eruption archive for IASI/Metop-B

270 The time series of the SO<sub>2</sub> detections derived from the IASI-PCA-GE method is applied to IASI/Metop-B global  
271 dataset over the 2013-2022 period. Figure 7 shows the comparison of the SO<sub>2</sub> IASI-PCA-GE signal intensity with the  
272 SO<sub>2</sub> hyperspectral range indexes (HRI) product at 5 km (Bauduin et al., 2016). HRIs at 5 km are chosen because of a  
273 good sensitivity around this altitude (Clarisse et al., 2014) compared to L2 SO<sub>2</sub> concentration data that are showing  
274 concentration above 5 km (likely the high intensity volcanism). Only daily SO<sub>2</sub> extrema of both the IASI-PCA-GE  
275 method and HRI product are compared. They are spatially co-located and associated with documented volcanic events  
276 from the Global Volcanism Program, Smithsonian Institution (<https://volcano.si.edu/>). It is observed that both methods  
277 are able to detect not only intense eruptions but also moderate or degassing volcanic events. The largest volcanic  
278 eruptions detected during this period for both methods are Calbuco on 22 April 2015, Raikoke on 22 June 2019 and  
279 Ubinas on 19 July 2019 (Sennert, 2015, 2019, 2019b). Furthermore, for all major events (corresponding to 2810 days  
280 over 3373 days in total), an excellent correlation between HRI and IASI-PCA-GE signal intensity ( $R^2 = 0.96$ ) is found  
281 between the two datasets.



282

283 **Figure 7: Time series of SO<sub>2</sub> detections from IASI-PCA-GE method (grey) and the SO<sub>2</sub> HRI at 5 km (orange) based on the**  
284 **IASI/Metop-B L1C data for the 2013-2022 period. Only the daily extrema are shown in the time series.**

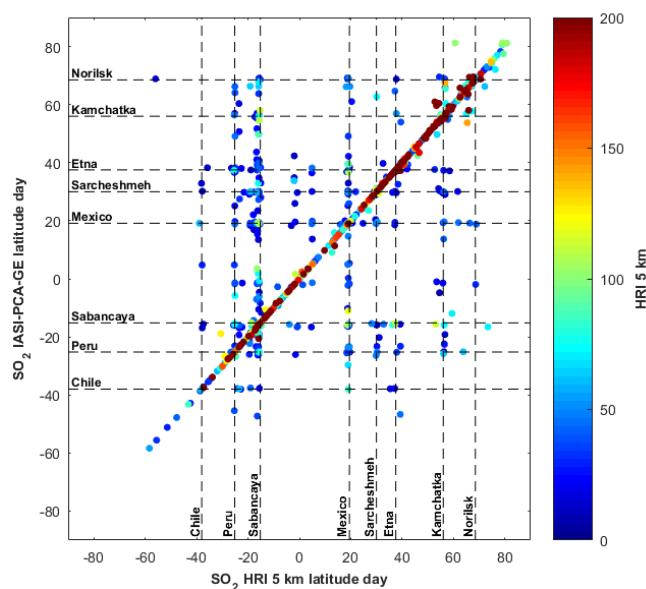
285 In order to analyse and understand the differences between the two records, the correlation between the latitudes of  
286 both datasets shown in Fig. 7 are plotted (see Figure 8). An excellent location correlation between both HRI and IASI-  
287 PCA-GE methods is observed for high intensity detections. However, some discrepancies are found in case of low  
288 intensity events, corresponding to commonly active degassing volcanoes.

289 Some specific latitudes associated with degassing volcanoes such as Sabancaya (Moussallam et al., 2017), the Vanuatu  
290 island arc with Ambae (Ani et al., 2012), Colima and Popocatepetl in Mexico (Varley et al., 2003) and the long eruptive  
291 Kilauea volcano (Garcia et al., 2021) respectively at 15.8° S, 15.4° S, 19.5° N, 19.0° N and 19.4° N are illustrated by  
292 the black horizontal and vertical dashed lines in Fig. 8. Furthermore, some daily maxima are located around 38° S,  
293 37.5° N and 25.2° N and are respectively related to emissions from Copahue (Reath et al., 2019), Etna (Tamburello et  
294 al., 2013 ; Ganci et al., 2012) and several Chilean volcanoes.

295 The daily maxima located around 56° N are investigated and found to be associated with Kamchatka degassing  
296 volcanoes. Disperse latitudes of IASI-PCA-GE daily maxima are not consistent with the colocated HRI maxima. These  
297 differences between the IASI-PCA-GE and HRI methods can also be explained by the relation between plume  
298 altitude/temperature not represented in the principal components that will also affect the spectral reconstruction. As a  
299 result the location of daily maxima can be different in case of low intensity detections because of the PCA  
300 overestimation (or underestimation) of atmospheric anomalies. This also results on a non-linearity between retrieved  
301 concentrations and PCA intensities.



302 It is interesting to note that both IASI-PCA-GE and HRI detections observed at around 30° N and 65° N are associated  
303 with anthropogenic emissions in the region of Sarcheshmeh Copper, one of largest industrial-mining complexes for  
304 Copper that is emitting about 789.9 tons of SO<sub>2</sub> per day (Amirtaimoori et al., 2014) and over the Norilsk city, also well  
305 know for its mining and smelting industries (Bauduin et al., 2016). That finding illustrates the capacity of both methods  
306 to detect industrial emissions.



307

308 **Figure 8: Comparison of latitudes corresponding to the daily maxima detected for both IASI-PCA-GE SO<sub>2</sub> signal intensity**  
309 **and HRI product between 2013 and 2022 with IASI-B L1C data during the day. The dashed lines show location**  
310 **discrepancies.**

311 It is found that the relation between concentration and signal intensity is not linear and the PCA-based results cannot  
312 be used for an accurate quantification of SO<sub>2</sub> concentrations. Indeed, IASI-PCA-GE signals will be dependent on the  
313 molecule concentration but also on thermal contrast, and other surface parameters and atmospheric conditions. This  
314 is why discrepancies are found at high latitudes between location of IASI-PCA-GE and HRI maxima, which are  
315 associated with eruptions in the Kamchatka region.

## 316 5.2 Fire events

317 Fires can be a significant source of trace gases and aerosols in the atmosphere and several species were specifically  
318 researched in fire events: CO, NH<sub>3</sub>, formic acid (HCOOH), acetylene (C<sub>2</sub>H<sub>2</sub>), ethylene (C<sub>2</sub>H<sub>4</sub>), nitrous acid (HONO),  
319 ethane (C<sub>2</sub>H<sub>6</sub>), acetonitrile (CH<sub>3</sub>CN), methanol (CH<sub>3</sub>OH), peroxyacetyl nitrate (CH<sub>3</sub>CO(OONO<sub>2</sub>)), hydrogen cyanide  
320 (HCN), formaldehyde (HCHO), glyoxal (CHOCHO), and CH<sub>4</sub> (Li et al., 2000; Goode et al., 2000; Sharpe et al., 2004;  
321 Coheur et al., 2009; Dufлот et al., 2013; R'Honi et al., 2013; Zarzana et al., 2018, De longueville et al., 2021). The

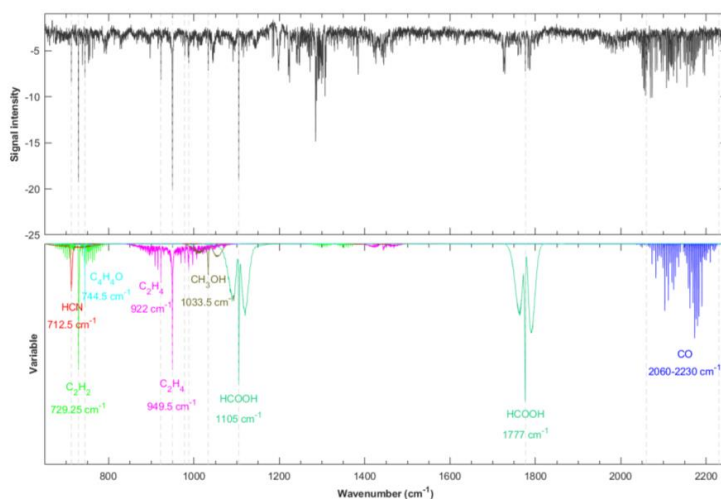


322 IASI-PCA-GE method was applied to several case studies, but only one is presented here, selected during the fire  
323 season occurring in Australia in 2019-2020.

### 324 5.2.1 The Australia case study

325 In Australia, fire events known as bushfires are occurring every year. Coupled with global warming and the lack of  
326 rainfall in 2019-2020, the fires were particularly intense with burned areas covering more than 186 000 km<sup>2</sup>. It was  
327 shown that pyroconvection allowed the plume to reach the lower stratosphere around 15-16 km (Khaykin et al., 2020).  
328 Many species were observed by ACE-FTS during that episode (e.g., Boone et al., 2020): CO, C<sub>2</sub>H<sub>6</sub>, C<sub>2</sub>H<sub>2</sub>, HCN,  
329 HCOOH, CH<sub>3</sub>OH, PAN, acetone (CH<sub>3</sub>COCH<sub>3</sub>) and CH<sub>3</sub>CN.

330 The IASI-PCA-GE method was applied to the IASI/Metop-B L1C data on 1 January 2020. Figure 9 illustrates an  
331 example of a normalized GMI pseudo spectrum obtained during the Australia fire event. As expected, peaks relative  
332 to the CO absorption lines are found in the 2050-2200 cm<sup>-1</sup> spectral domain. Other peaks associated with the absorption  
333 of molecules are also visible: HCN with a peak at 712.5 cm<sup>-1</sup>, furan (C<sub>4</sub>H<sub>4</sub>O) at 744.5 cm<sup>-1</sup>, C<sub>2</sub>H<sub>2</sub> at 729.25 cm<sup>-1</sup>, C<sub>2</sub>H<sub>4</sub>  
334 at 949.5 cm<sup>-1</sup>, HCOOH at 1105 cm<sup>-1</sup> and 1777 cm<sup>-1</sup>, CH<sub>3</sub>OH at 1033.5 cm<sup>-1</sup>, as well as peaks associated with NH<sub>3</sub> at  
335 around 931 cm<sup>-1</sup> and 967 cm<sup>-1</sup>.



336

337 **Figure 9: Top: Example of GMI pseudo spectrum calculated from IASI/Metop-B L1C data during the intense fire event in**  
338 **Australia on 1 January 2020 in the morning (AM orbit). Bottom: HITRAN spectroscopic parameter associated with the**  
339 **absorption of different species are shown in colours.**

340 Figure 10 (left column) shows the spatial distribution of the residual values associated with the detected species in the  
341 GMI pseudo spectrum. Despite their different lifetimes, the plumes for the different species are located in the same  
342 region (around 180° E in the Pacific Ocean).

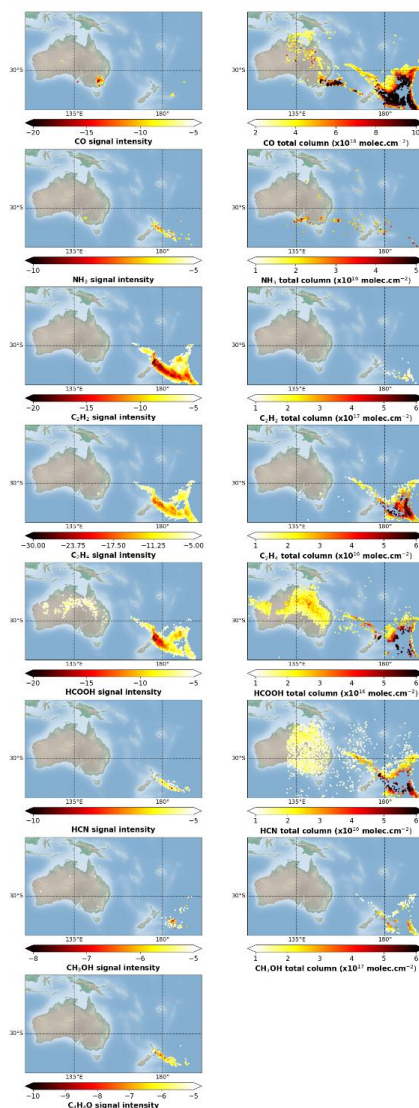
343 Carbon monoxide is retrieved in near real time (George et al., 2009) from IASI L1C and is used for monitoring fires  
344 (Turquety et al., 2009). In Fig. 10, CO is both observed both with the IASI-PCA-GE and retrieval methods. However,



345 some discrepancies are found in terms of location and intensity. A few pixels are detected by the IASI-PCA-GE method  
346 in the Southeast of Australia, which is in agreement with the CO operational L2 product. However, the retrieval method  
347 is able to detect a larger plume over Australia compared to the IASI-PCA-GE method. Furthermore, a large plume is  
348 also detected over the Pacific Ocean but is missed by the IASI-PCA-GE method. Note that, the high intensity CO  
349 peaks are clearly detected in the residuals (c.f. Fig. 10). However, most of the missing pixels, in the PCA detection  
350 results, are located above sea. That could be due to the combination between the database chosen in the PCA method  
351 and the spectral domain high variability. Indeed, a higher thermal contrast variability is observed above land (Clerbaux  
352 et al., 2009), but the database contains spectra representing the natural variability without differencing sea and land  
353 pixels. As a result, the spectral reconstruction above sea with the PCA method will be less sensitive to spectral  
354 variations, causing a reduced sensitivity above sea. Furthermore, the spectral region between 2050 and 2200  $\text{cm}^{-1}$  has  
355 shown a large statistical distribution of extrema signals within the 21500 granules used for threshold calculation in  
356 Section 4.2 allowing to set a restrictive threshold for the outlier detection for CO. That restrictive will also impact the  
357 number of detected pixels. The sensitivity of PCA reconstruction outliers to strong CO concentrations in fires should  
358 be more deeply investigated in further studies.

359  $\text{NH}_3$  is also retrieved in near real time (Van Damme et al., 2017) and observed in low concentration and occurrence  
360 above Australia on the 1<sup>st</sup> January 2020 in the L2 retrievals and in low signal and occurrence in the IASI-PCA-GE  
361 method. Some pixels are detected by the IASI-PCA-GE method but are not spatially correlated with the  $\text{NH}_3$  total  
362 column L2 data. A weak detection of  $\text{NH}_3$  is expected since only low intensity peaks of  $\text{NH}_3$  are found in the GMI  
363 pseudo spectrum but two plumes are observed above both land and sea while L2 retrievals only show many isolated  
364 pixels.

365 However, for other indicators the size of the plume differs: large plumes are found for  $\text{C}_2\text{H}_2$ ,  $\text{C}_2\text{H}_4$  and  $\text{HCOOH}$  while  
366 smaller plumes are found for  $\text{HCN}$ ,  $\text{C}_4\text{H}_4\text{O}$  and  $\text{CH}_3\text{OH}$ . Those differences can be explained by the difference between  
367 both methods. Indeed, the column maps includes the effects of radiative transfer (thermal contrast in particular), and  
368 the presence of clouds can also induce differences between both products as the retrievals are highly sensitive to clouds.  
369 For the IASI-PCA-GE method, the sensitivity for molecules detection highly depends on the selection of spectra to  
370 construct the database and the thresholds chosen for the detection.



371

372 **Figure 10: Left: Spatial distribution of the residual values associated with CO, NH<sub>3</sub>, HCN, C<sub>2</sub>H<sub>2</sub>, C<sub>2</sub>H<sub>4</sub>, CH<sub>3</sub>OH, HCOOH**  
373 **and C<sub>4</sub>H<sub>4</sub>O detections from IASI/Metop-B L1C data during the intense fire event in Australia on 1 January 2020 in the**  
374 **morning (AM orbit); right: same as left for the total column L2 data. There is no map of C<sub>4</sub>H<sub>4</sub>O total column L2 data**  
375 **because there is no retrieval available.**

### 376 5.2.2 Fire archive for IASI/Metop-B

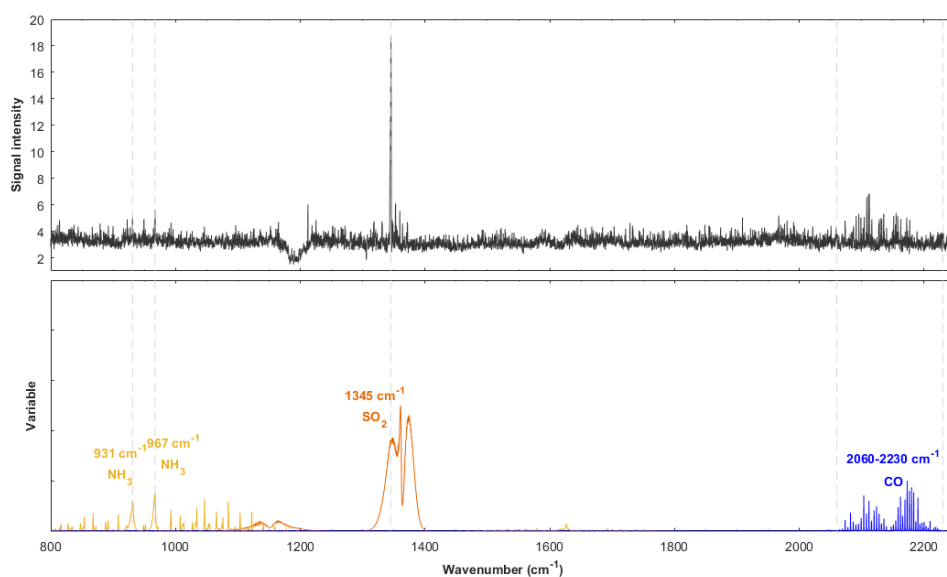
377 Figure 11 illustrates the time series of the ethylene detections from IASI-PCA-GE method based on the IASI/Metop-  
378 B L1C data for the 2013–2022 period. C<sub>2</sub>H<sub>4</sub> is a weak absorber often detected around 949 cm<sup>-1</sup> in case of high intensity  
379 fires and is able to show many high intensity peaks attributed to fire events. In the figure, the most intense fires are







401 for domestic heating. The IASI-PCA-GE method was applied on 13 January 2013 during nighttime. The normalized  
402 GMA pseudo spectrum obtained during the China anthropogenic pollution is illustrated in Fig. 12. In order to optimize  
403 the sensitivity of the method for a low intensity event, the  $F_3$  thresholds were defined as  $F_3 = 5$  for both day and  
404 nighttime condition for the three species of interest (CO, NH<sub>3</sub> and SO<sub>2</sub>). We clearly see a signal associated with CO,  
405 NH<sub>3</sub>, and SO<sub>2</sub> spectral emission, with the largest signal for SO<sub>2</sub> (value reaching ~18). The detection of SO<sub>2</sub> around  
406 1345 cm<sup>-1</sup> is low compared to similar detection of SO<sub>2</sub> during volcanic eruptions. This result suggests that the SO<sub>2</sub>  
407 absorption bands around 1345 cm<sup>-1</sup> also allows the detection of SO<sub>2</sub> during anthropogenic pollution episodes, which  
408 is in agreement with the finding of Bauduin et al. (2014, 2016). Finally, the spectral feature around 1180-1200 cm<sup>-1</sup>  
409 showing a low signal intensity is likely due to the IASI detector band 1 – band 2 inter-band domain that is well captured  
410 in the IASI-PCA-GE method and should not be associated to an atmospheric absorption component.



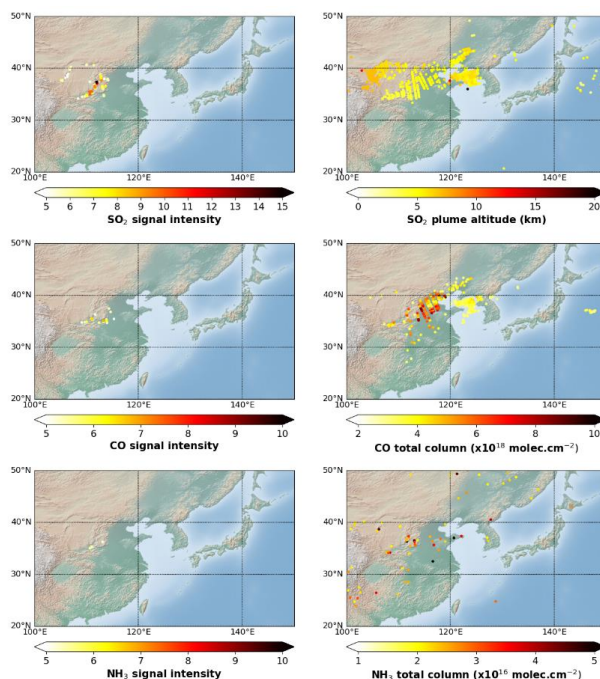
411  
412 **Figure 12: Top: Example of GMA pseudo spectrum calculated from IASI/Metop-A L1C data during an anthropogenic**  
413 **pollution event occurring in China on 13 January 2013 in the evening (PM orbit). Bottom: HITRAN spectroscopic**  
414 **parameter associated with the absorption of different species are shown in colours.**

415 The spatial distribution of the residual values associated with the detected species in the GMA pseudo spectrum (see  
416 Figure 12) is presented in Fig. 13 (left). The IASI-PCA-GE method allows the spectral detection of NH<sub>3</sub>, SO<sub>2</sub>, and CO.  
417 However only a few pixels are detected for NH<sub>3</sub>, which is due to the very low (<5) signal intensity found for that  
418 species. We see the same behavior for CO. However, a clear SO<sub>2</sub> plume characterized by a signal reaching ~18 (at  
419 1345 cm<sup>-1</sup> - see Fig. 12) is found by the IASI-PCA-GE method.

420 Figure 13 (right) illustrates the spatial distribution of NH<sub>3</sub> and CO total column and SO<sub>2</sub> plume altitude L2 data  
421 retrieved from the IASI/Metop-A L1C data (Clarisse et al., 2012). The retrieval and IASI-PCA-GE methods shows



422 different patterns. We clearly see two plumes for SO<sub>2</sub> plume altitude and CO concentrations, but only few pixels of  
423 detection are found for NH<sub>3</sub>.



424  
425 **Figure 13: Analysis of intense fire event in China on 13 January 2013 in the evening (PM orbit) based on IASI/Metop-A**  
426 **L1C data. Left plots: spatial distribution of residual values associated with SO<sub>2</sub>, CO and NH<sub>3</sub>. Right plot: SO<sub>2</sub> plume altitude**  
427 **retrievals (km), and CO and NH<sub>3</sub> total column retrievals (molec.cm<sup>-2</sup>).**

### 428 5.3.2 SO<sub>2</sub> released by a sulfur plant

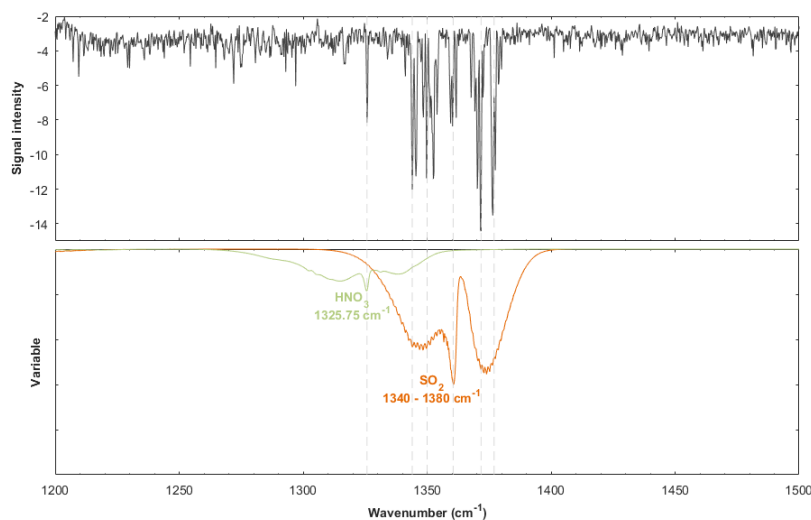
429 During the period extending from 20 October to 27 October 2016, a sulfur mine burnt in d’Al-Mishraq near Mosul,  
430 Iraq. This fire on the sulfur plant, which was set by Islamic state, caused a large emission of SO<sub>2</sub> and other sulfured  
431 species in the atmosphere, which was observed from several satellite instruments (Björnham et al., 2017). Similar plant  
432 fires occurred in June 2003 during four weeks with approximately 600 kt of SO<sub>2</sub> emitted (Carn et al., 2004). This was  
433 a major health hazard (Baird et al., 2012). Nearly thousand people were intoxicated due to toxic fire plumes, and two  
434 Iraqis died.

435 Figure 14 illustrates the normalized GMI pseudo spectrum obtained during the Iraq industrial disaster on 24 October  
436 2016 PM. The GMI pseudo spectrum is characterized by an absorption peak associated with HNO<sub>3</sub> artefact at ~1325.75  
437 cm<sup>-1</sup> and two absorption peaks associated with SO<sub>2</sub> at 1345 cm<sup>-1</sup> and 1371 cm<sup>-1</sup>. The signal intensity is about -14 for  
438 SO<sub>2</sub> which suggests that the event is of a low-medium intensity. However, the SO<sub>2</sub> peaks found at 1371 cm<sup>-1</sup> and 1377  
439 cm<sup>-1</sup> are mostly seen in case of intense volcanic eruptions, suggesting that the SO<sub>2</sub> concentrations are larger than



440 concentrations found above most of degassing volcanoes. This suggestion is well supported by Fig. 15 showing SO<sub>2</sub>  
441 total column up to 5 DU.

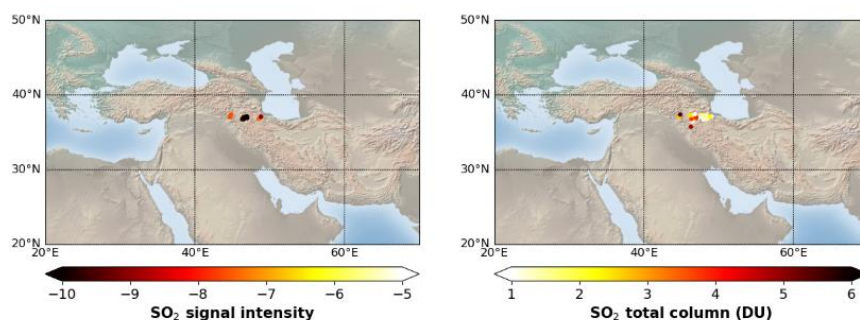
442 The presence of the artefact at 1325.75 cm<sup>-1</sup> can be explained by the reconstruction error in the 1300-1400 cm<sup>-1</sup> and  
443 contribution of SO<sub>2</sub> and aerosols as observe in the case of Ubinas eruption (see section 5.1.1). As the event is less  
444 intense than volcanic eruption, HNO<sub>3</sub> lower peaks around 750-950 cm<sup>-1</sup> are not observable.



445

446 **Figure 14: Top: Example of GMI pseudo spectrum calculated from IASI/Metop-B LIC data during a sulphur plant fire**  
447 **event occurring in Iraq on 24 October 2016 in the evening (PM orbit). Bottom: HITRAN spectroscopic parameter associated**  
448 **with the absorption of different species are shown in colours.**

449 The spatial distribution of the residual values associated with SO<sub>2</sub> detections is illustrated in Fig. 15. The IASI-PCA-  
450 GE method allows the spectral detection of this molecule in the region of interest four days after the fire started showing  
451 the transport of the plume on the east part of the country. Less pixels are detected by the IASI-PCA-GE method than  
452 by the L2 retrieval method. This can be explained by the fact that SO<sub>2</sub> thresholds associated with the IASI-PCA-GE  
453 method were empirically chosen to minimize false positive detections, and thus the detections of low intensity residuals  
454 can be missed.

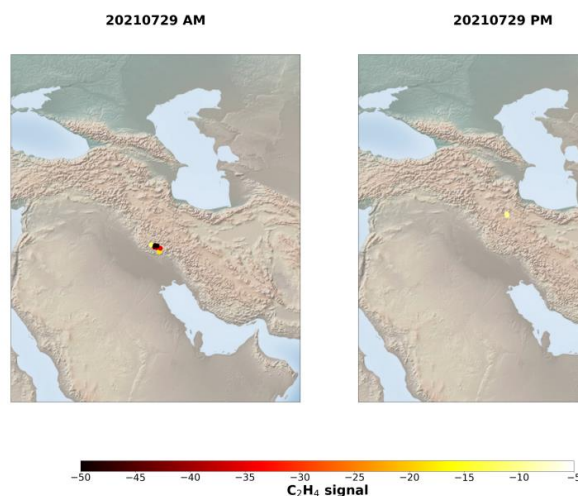


455

456 **Figure 15: Analysis of sulphur plant fire event in Iraq on 24 October 2016 in the evening (PM orbit) based on IASI/Metop-**  
457 **A L1C data. Left plot: spatial distribution of residual values associated with SO<sub>2</sub>. Right plot: SO<sub>2</sub> total column in Dobson**  
458 **Unit.**

### 459 5.3.3 C<sub>2</sub>H<sub>4</sub> sporadic emission at the border of Iran/Iraq

460 In Section 5.2.2 we reported that the IASI-PCA-GE method is well suited to detect biomass burning by using the C<sub>2</sub>H<sub>4</sub>  
461 indicator, found in conjunction with other signatures of molecules usually associated with fire activity. Among the  
462 events that we inventoried, on a few occasions, we found intense signatures in the Iran/Iraq region with no other  
463 absorption than C<sub>2</sub>H<sub>4</sub>, which suggests that sources other than biomass burning – likely due to anthropogenic activities  
464 – are at play. The main event occurred in July 2021 and some other weaker ones are also identified in Fig. 11. By  
465 averaging IASI data over time and using a supersampling technique, Franco et al. (2022) exposed and identified over  
466 300 worldwide emitters of C<sub>2</sub>H<sub>4</sub>, emanating from petrochemical clusters, steel plants, coal-related industries, and  
467 megacities. However, no C<sub>2</sub>H<sub>4</sub> point source was formally identified in this Iran/Iraq region. But the method described  
468 in this paper is well suited to also detect sporadic events, which contrasts with the continuous emissions exposed by  
469 Franco et al. (2022). Indeed, oversampling methods are well suited for the detection of regular, even weak,  
470 anthropogenic sources, but typically miss transient sources lasting for less than 24 hours. A new analysis was therefore  
471 performed on the events spotted by the IASI-PCA-GE method, which led to the identification of plumes lasting for  
472 only a few hours (see Figure 16), for specific days as identified on Fig. 11. Although visible satellite imagery and  
473 independent online information indicate the presence of oil and gas activities in that area, no firm identification was  
474 possible, and further investigation is needed to identify the potential sources of these sporadic emissions.



475

476 **Figure 16: Analysis of acetylene sporadic emission event in Iraq on 29 July 2021 based on IASI/Metop-A LIC data. Left**  
477 **plot: spatial distribution of residual values associated with C<sub>2</sub>H<sub>4</sub> during the morning orbit. Right plot: spatial distribution**  
478 **of residual values associated with C<sub>2</sub>H<sub>4</sub> during the evening orbit.**

## 479 **6 Conclusions and perspectives**

480 This paper presents an innovative approach, based on a PCA method applied on the IASI radiance, allowing the  
481 detection and characterization of exceptional events in near real time. This new method, the IASI-PCA granule extrema  
482 (GE) method, consists in focusing on extrema calculated within a geographical region. A statistical selection is made  
483 for focusing on abnormal variability in IASI channels (detection of outliers) in order to detect the contribution of  
484 specific molecules from different types of events. It is applied to the three-minute granule of IASI observations  
485 allowing the near real time detection of a series of short-lived trace gases.

486 Using a dataset representing the full range of atmospheric conditions, we show that the PCA method is well suited to  
487 efficiently detect outliers. The analysis of the outliers allows the identification of spectral features exceeding the natural  
488 variability of several absorbing species especially for weak absorbers, emitted during fires, volcanic, anthropogenic  
489 pollution, or industrial disaster. The method is more robust than previous retrieval methods when the spectra are cloud-  
490 contaminated.

491 The analysis of several case studies shows a good sensitivity of the IASI-PCA-GE method, which is able to detect  
492 weak absorbers such as SO<sub>2</sub>, HCN, C<sub>2</sub>H<sub>2</sub>, C<sub>2</sub>H<sub>4</sub>, CH<sub>3</sub>OH, C<sub>4</sub>H<sub>4</sub>O and NH<sub>3</sub>. We also showed that the method is well  
493 suited to detect transient events that last only a few hours/days.

494 Our work shows that within a granule the negative part of residuals (GMI) contains more information than the positive  
495 represented by the GMA. However, the latter contains relevant information in case of negative thermal contrasts,  
496 allowing the detection of specific events such as the recurrent anthropogenic pollution events occurring in China in  
497 winter.



498 The IASI-PCA-GE method is better suited to detect short-lived species and only species characterized by spectral  
499 absorption lines are defined in the method. Species such as PAN, CH<sub>3</sub>COOH and CH<sub>3</sub>COCH<sub>3</sub> characterized by a  
500 broadband absorption are more difficult to detect with the IASI-PCA-GE method. Less conclusive results were  
501 obtained for CO which has a lower atmospheric concentration variability because of its longer lifetime. This could also  
502 be related to the training database used in this study, which still contains outliers impacting the sensitivity. In a next  
503 version, the method will be optimized by removing the outliers still present in the database. Furthermore, as the PCA  
504 detection depends on different geophysical parameters such as the temperature, thermal contrast or the construction of  
505 the principal component basis, the detection of most extreme cases of concentration anomalies is possible but the  
506 sensitivity of the method will depend on the latitude of observations. Added to that, in case of intense volcanic eruption,  
507 some signal artefacts can appear due to the high reconstruction error observed in the 1300-1400 cm<sup>-1</sup>.

508 Finally, this paper shows the capacity of PCA detection to detect different species from an event to another, especially  
509 in case of fire events, which suggest the possibility to categorize fire events based on judicious combinations of species.  
510 The method also proves useful to derive consistent records for fire and volcanic events, and data will continue to  
511 accumulate over time as the method is now routinely implemented. Further work is still needed to avoid false  
512 detections, such as those associated with HNO<sub>3</sub> which are due to the correlation between different absorption bands  
513 for the same molecule, likely interfering with SO<sub>2</sub> present in the plumes.

#### 514 **Data availability statement**

515 The IASI L2 SO<sub>2</sub> (SO<sub>2</sub>, NH<sub>3</sub>, CO, HCOOH data can be downloaded from the Aeris portal <https://iasi.aeris-data.fr/SO2/>  
516 (<https://doi.org/10.25326/42>); <https://iasi.aeris-data.fr/nh3/> (<https://doi.org/10.25326/10>); <https://iasi.aeris-data.fr/CO/>  
517 (<https://doi.org/10.25326/64>); <https://iasi.aeris-data.fr/hcooh/> (<https://doi.org/10.25326/15>)). The VOC retrievals  
518 (CH<sub>3</sub>OH and HCOOH: <https://doi.org/10.1029/2018JD029633>; HCN: <https://doi.org/10.5194/acp-21-11257-2021>) are  
519 processed by Franco Bruno at ULB ([bruno.franco@ulb.be](mailto:bruno.franco@ulb.be)).

#### 520 **Acknowledgments**

521 A. Vu Van acknowledges funding from SPACIA SA through an ANRT CIFRE PhD grant. IASI is a joint mission of  
522 EUMETSAT and the Centre National d'Etudes Spatiales (CNES, France). The IASI Level 1C data are distributed in  
523 near real time by EUMETSAT through the EUMETCast system distribution. The authors acknowledge the AERIS  
524 data infrastructure (<https://www.aeris-data.fr>) for providing access to the IASI Level 1 radiance and Level 2  
525 concentration data used in this study, and CNES for financial support.

526

527

528

529

530



531 **Appendix**

532 **Table A1: Infrared absorption spectral ranges used for the detection of molecular absorptions.**

Computed spectral range (cm <sup>-1</sup> )	Width (cm <sup>-1</sup> )	Molecule	Infrared absorption peaks	References
711.50 - 713.50	2.00	HCN	712.5 cm <sup>-1</sup> (Q-branch)	(Gordon et al., 2017, 2022)
729.25 - 730.00	0.75	C <sub>2</sub> H <sub>2</sub>	729.25 cm <sup>-1</sup> (Q-branch ν <sub>3</sub> band)	(Gordon et al., 2017, 2022)
744.25 - 744.75	0.50	C <sub>4</sub> H <sub>4</sub> O	744.5 cm <sup>-1</sup> (ν <sub>20</sub> band)	(Gordon et al., 2017, 2022)
763.00 - 763.75	0.75	HNO <sub>3</sub>	763 cm <sup>-1</sup> (Q-branch ν <sub>8</sub> band)	(Gordon et al., 2017, 2022)
790.25 - 790.75	0.50	HONO	790 cm <sup>-1</sup> (Q-branch trans-ν <sub>4</sub> band)	(Barney et al., 2000)
853.50 - 854.25	0.75	NH <sub>3</sub>	854 cm <sup>-1</sup> (Q-branch)	(Gordon et al., 2017, 2022)
867.75 - 868.75	1.00	NH <sub>3</sub>	868 cm <sup>-1</sup> (Q-branch)	(Gordon et al., 2017, 2022)
878.50 - 880.00	1.50	HNO <sub>3</sub>	879 cm <sup>-1</sup> (Q-branch ν <sub>5</sub> band)	(Gordon et al., 2017, 2022)
887.25 - 888.25	1.00	NH <sub>3</sub>	888 cm <sup>-1</sup> (Q-branch)	(Gordon et al., 2017, 2022)
891.75 - 892.25	0.50	NH <sub>3</sub>	892 cm <sup>-1</sup> (Q-branch)	(Gordon et al., 2017, 2022)
895.50 - 896.75	1.25	HNO <sub>3</sub>	896 cm <sup>-1</sup> (Q-branch 2ν <sub>9</sub> band)	(Gordon et al., 2017, 2022)
908.00 - 909.00	1.00	NH <sub>3</sub>	908.25 cm <sup>-1</sup> (Q-branch)	(Gordon et al., 2017, 2022)
931.75 - 933.75	2.00	NH <sub>3</sub>	930 cm <sup>-1</sup> (Q-branch)	(Gordon et al., 2017, 2022)
949.00 - 950.50	1.50	C <sub>2</sub> H <sub>4</sub>	949 cm <sup>-1</sup> (Q-branch ν <sub>7</sub> band)	(Gordon et al., 2017, 2022)
966.00 - 968.00	2.00	NH <sub>3</sub>	967 cm <sup>-1</sup> (Q-branch)	(Gordon et al., 2017, 2022)
991.75 - 993.50	1.75	NH <sub>3</sub>	992.75 cm <sup>-1</sup> (Q-branch)	(Gordon et al., 2017, 2022)
1007.75 - 1008.25	0.50	NH <sub>3</sub>	1008 cm <sup>-1</sup> (Q-branch)	(Gordon et al., 2017, 2022)
1033.00 - 1033.75	0.75	CH <sub>3</sub> OH	1033.5 cm <sup>-1</sup> (Q-branch)	(Razavi et al., 2011)
1034.00 - 1034.25	0.25	NH <sub>3</sub>	1034 cm <sup>-1</sup> (Q-branch)	(Gordon et al., 2017, 2022)
1046.25 - 1047.25	1.00	NH <sub>3</sub>	1047 cm <sup>-1</sup> (Q-branch)	(Gordon et al., 2017, 2022)
1065.75 - 1066.25	0.50	NH <sub>3</sub>	1066 cm <sup>-1</sup> (Q-branch)	(Gordon et al., 2017, 2022)
1075.75 - 1076.25	0.50	NH <sub>3</sub>	1076 cm <sup>-1</sup> (Q-branch)	(Gordon et al., 2017, 2022)
1084.50 - 1085.75	1.25	NH <sub>3</sub>	1085 cm <sup>-1</sup> (Q-branch)	(Gordon et al., 2017, 2022)
1103.00 - 1104.25	1.25	NH <sub>3</sub>	1104 cm <sup>-1</sup> (Q-branch)	(Gordon et al., 2017, 2022)
1104.50 - 1105.75	1.25	HCOOH	1105 cm <sup>-1</sup> (Q-branch ν <sub>6</sub> band)	(Gordon et al., 2017, 2022)
1121.50 - 1122.75	1.25	NH <sub>3</sub>	1122 cm <sup>-1</sup> (Q-branch)	(Gordon et al., 2017, 2022)
1325.75 - 1326.25	0.50	HNO <sub>3</sub>	1326 cm <sup>-1</sup> (ν <sub>3</sub> band)	(Gordon et al., 2017, 2022)
1344.50 - 1346.50	1.00	SO <sub>2</sub>	1345 cm <sup>-1</sup> (ν <sub>3</sub> band)	(Gordon et al., 2017, 2022)
1370.50 - 1372.00	1.50	SO <sub>2</sub>	1371 cm <sup>-1</sup> (ν <sub>3</sub> band)	(Gordon et al., 2017, 2022)
1375.75 - 1377.00	1.25	SO <sub>2</sub>	1376 cm <sup>-1</sup> (ν <sub>3</sub> band)	(Gordon et al., 2017, 2022)
1710.75 - 1711.50	0.75	HNO <sub>3</sub>	1711 cm <sup>-1</sup> (Q-branch)	(Gordon et al., 2017, 2022)
1776.75 - 1777.25	0.50	HCOOH	1777 cm <sup>-1</sup> (ν <sub>3</sub> band)	(Gordon et al., 2017, 2022)
2111.00 - 2112.25	1.25	CO	2111.50 cm <sup>-1</sup> (P-branch)	(Hadji-Lazaro, 1999)
2123.00 - 2124.25	1.25	CO	2123.75 cm <sup>-1</sup> (P-branch)	(Hadji-Lazaro, 1999)
2130.00 - 2132.25	2.25	CO	2131.75 cm <sup>-1</sup> (P-branch)	(Hadji-Lazaro, 1999)
2157.75 - 2158.75	1.00	CO	2158.00 cm <sup>-1</sup> (R-branch)	(Hadji-Lazaro, 1999)
2164.75 - 2166.00	1.25	CO	2165.75 cm <sup>-1</sup> (R-branch)	(Hadji-Lazaro, 1999)

533





## 534 References

- Ackerman S. A., Strabala K. I.: Satellite remote-sensing of H<sub>2</sub>SO<sub>4</sub> aerosol using the 8 to 12 mm window region: Application to Mount Pinatubo, *J. Geophys. Res.*, 99(D9), 18,639 – 18,649, doi:10.1029/94JD01331, 1994.
- Amirtaimoori S., Khalilian S., Amirnejad H., Mohebbi A.: Estimation of cost curve to control sulfur dioxide gas (SO<sub>2</sub>) emissions from sarcheshmeh copper complex. *Journal of Environmental Studies*. 40. 431-438, 2014.
- Ani P., Oppenheimer C., Allard P., Shinohara H., Tsanev V. et al.: First estimate of volcanic SO<sub>2</sub> budget for Vanuatu island arc. *Journal of Volcanology and Geothermal Research*, Elsevier, 2012, 211-212, pp.36-46. 10.1016/j.jvolgeores.2011.10.005. insu-00638268, 2012.
- Atkinson N. C., Brunel P., Marguinaud P., Labrot T.: AAPP developments and experiences with processing METOP data, *Tech. Proc. 16th Int. TOVS Study Conf.*, Angra dos Reis, Brazil, 6–13 May, 2008.
- Atkinson N. C., Hilton F. I., Illingworth S. M., Eyre J. R., Hultberg, T.: Potential for the use of reconstructed IASI radiances in the detection of atmospheric trace gases, *Atmos. Meas. Tech.*, 3, 991–1003, <https://doi.org/10.5194/amt-3-991-2010>, 2010.
- Baird C.P., Debakey S., Reid L., Hauschild V.D., Petrucci B., Abraham J.H.: Respiratory health status of US army personnel potentially exposed to smoke from 2003 Al-Mishraq sulfur plant fire *J. Occup. Environ. Med.*, 54 (2012), pp. 717-723, 2012.
- Bauduin S., Clarisse L., Clerbaux C., Hurtmans D. and Coheur P.-F.: IASI observations of sulfur dioxide (SO<sub>2</sub>) in the boundary layer of Norilsk, *Journal of Geophysical Research : Atmospheres*, 119, 4253–4263, <https://doi.org/10.1002/2013JD021405>, 2014.
- Bauduin S., Clarisse L., Hadji-Lazaro J., Theys N., Clerbaux C. and Coheur P.-F.: Retrieval of near-surface sulfur dioxide (SO<sub>2</sub>) concentrations at a global scale using IASI satellite observations, *Atmospheric Measurement Techniques*, 9, 721-740, <https://doi.org/10.5194/amt-9-721-2016>, 2016.
- Barney W.S., Wingen L.M., Lakin M.J., Brauers T., Stutz J., Finlayson-Pitts B.J.: Infrared Absorption Cross-Section Measurements for Nitrous Acid (HONO) at Room Temperature, *J. Phys. Chem. A* 2000, 104, 1692-1699, 2000.
- Björnham O., Grahn H., Von Schoenberg P., Liljedahl B., Waleij A., Brännström N.: The 2016 Al-Mishraq sulphur plant fire: Source and health risk area estimation, *Atmospheric Environment*, Volume 169, 2017, Pages 287-296, ISSN 1352-2310, <https://doi.org/10.1016/j.atmosenv.2017.09.025>, 2017.
- Boone C. D., Bernath P. F., Fromm M. D.: Pyrocumulonimbus stratospheric plume injections measured by the ACE-FTS. *Geophysical Research Letters*, 47, e2020GL088442. <https://doi.org/10.1029/2020GL088442>, 2020.
- Boynard A, Clerbaux C, Clarisse L., Safieddine S., Pommier M., M. Van Damme M., Bauduin S., Oudot C., Hadji-Lazaro J., Hurtmans D., Coheur P.-F., First simultaneous space measurements of atmospheric pollutants in the boundary layer from IASI: a case study in the North China Plain *Geophys. Res. Lett.*, 41 (2014), pp. 645-651, 2014.



Capelle V., Chédin A., Siméon M., Tsamalis C., Pierangelo C., Pondrom M., Crevoisier C., Crepeau L., and Scott N. A.: Evaluation of IASI-derived dust aerosol characteristics over the tropical belt, *Atmos. Chem. Phys.*, 14, 9343–9362, <https://doi.org/10.5194/acp-14-9343-2014>, 2014.

Carn S., Krueger A., Krotkov N., Gray M.: Fire at Iraqi sulfur plant emits SO<sub>2</sub> clouds detected by earth probe TOMS, *Geophys. Res. Lett.*, 31, 2004.

Clarisse L., Coheur P-F., Prata A.J., Hurtmans D., Razavi A., et al.: Tracking and quantifying volcanic SO<sub>2</sub> with IASI, the September 2007 eruption at Jebel at Tair. *Atmospheric Chemistry and Physics*, European Geosciences Union, 2008, 8 (24), pp.7723-7734. hal-00349230, <https://doi.org/10.5194/acp-8-7723-2008>, 2008.

Clarisse L., Coheur P-F., Chefdeville S., Lacour J-L., Hurtmans D., et al.: Infrared satellite observations of hydrogen sulfide in the volcanic plume of the August 2008 Kasatochi eruption. *Geophysical Research Letters*, American Geophysical Union, 2011, 38 (10), pp. L10804. hal-00595308. <https://doi.org/10.1029/2011GL047402>, 2011.

Clarisse L., Hurtmans D., Clerbaux C., Hadji-Lazaro J., Ngadi Y., and Coheur P.-F.: Retrieval of sulphur dioxide from the infrared atmospheric sounding interferometer (IASI), *Atmos. Meas. Tech.*, 5, 581–594, <https://doi.org/10.5194/amt-5-581-2012>, 2012.

Clarisse L., Clerbaux C., Franco B., Hadji-Lazaro J., Whitburn S., Kopp A. K., et al.: A decadal data set of global atmospheric dust retrieved from IASI satellite measurements. *Journal of Geophysical Research: Atmospheres*, 124, 1618–1647. <https://doi.org/10.1029/2018JD029701>, 2019.

Clerbaux C., Boynard A., Clarisse L., George M., Hadji-Lazaro J., Herbin H., Hurtmans D., Pommier M., Razavi A., Turquety S., Wespes C., and Coheur P.-F.: Monitoring of atmospheric composition using the thermal infrared IASI/MetOp sounder, *Atmos. Chem. Phys.*, 9, 6041–6054, <https://doi.org/10.5194/acp-9-6041-2009>, 2009.

Coheur P.-F., Clarisse L., Turquety S., Hurtmans D., and Clerbaux C.: IASI measurements of reactive trace species in biomass burning plumes, *Atmos. Chem. Phys.*, 9, 5655–5667, <https://doi.org/10.5194/acp-9-5655-2009>, 2009.

Collard A.D., McNally A.P., Hilton F.I., Healy S.B. and Atkinson N.C.: The use of principal component analysis for the assimilation of high-resolution infrared sounder observations for numerical weather prediction. *Q.J.R. Meteorol. Soc.*, 136: 2038-2050. <https://doi.org/10.1002/qj.701>, 2010.

De Longueville H., Clarisse L., Whitburn S., Franco B., Bauduin S., Clerbaux C., Camy-Peyret C., Coheur P.-F.: Identification of Short and Long-Lived Atmospheric Trace Gases from IASI Space Observations, *Geophysical Research Letters*, 48, 5, (2021). <https://doi.org/10.1029/2020GL091742>, 2021.

Duflot, V., Hurtmans, D., Clarisse, L., R'honi, Y., Vigouroux, C., De Mazière, M., Mahieu, E., Servais, C., Clerbaux, C., and Coheur, P.-F: Measurements of hydrogen cyanide (HCN) and acetylene (C<sub>2</sub>H<sub>2</sub>) from the Infrared Atmospheric Sounding Interferometer (IASI), *Atmos. Meas. Tech.*, 6, 917–925, <https://doi.org/10.5194/amt-6-917-2013>, 2013.



Dufour G., Eremenko M., Beekmann M., Cuesta J., Foret G., et al.: Lower tropospheric ozone over the North China Plain: variability and trends revealed by IASI satellite observations for 2008–2016. *Atmospheric Chemistry and Physics*, European Geosciences Union, 2018, 18 (22), pp.16439-16459, 10.5194/acp-18-16439-2018, hal-02364072, 2018.

Franco B., Clarisse L., Stavrakou T., Müller J.-F., Van Damme M., Whitburn S., et al.: A general framework for global retrievals of trace gases from IASI: Application to methanol, formic acid, and PAN. *Journal of Geophysical Research: Atmospheres*, 123, 13,963– 13,984. <https://doi.org/10.1029/2018JD029633>, 2018.

Franco B., Clarisse L., van Damme M., Hadji-Lazaro J., Clerbaux C., Coheur P.-F., Ethylene industrial emitters seen from space, *Nature Communications*, Nature Publishing Group, 13, 6452. doi : 10.1038/s41467-022-34098-8, 2022.

Ganci G., Harris A. J. L., Del Negro C., Guehenneux Y., Cappello A., Labazuy P., Calvari S., and Gouhier M.: A year of lava fountaining at Etna: Volumes from SEVIRI, *Geophys. Res. Lett.*, 39, L06305, doi:10.1029/2012GL051026, 2012.

Garcia M. O., Pietruszka A. J., Norman M. D., Rhodes J. M.: Kīlauea's Pu'ū 'Ō'ō Eruption (1983–2018): A synthesis of magmatic processes during a prolonged basaltic event, *Chemical Geology*, Volume 581, 2021, 120391, ISSN 0009-2541, <https://doi.org/10.1016/j.chemgeo.2021.120391> , 2021.

García O. E., Sepúlveda E., Schneider M., Hase F., August T., Blumenstock T., Kühl S., Munro R., Gómez-Peláez Á. J., Hultberg T., Redondas A., Barthlott S., Wiegeler A., González Y., Sanromá E.: Consistency and quality assessment of the Metop-A/IASI and Metop-B/IASI operational trace gas products (O<sub>3</sub>, CO, N<sub>2</sub>O, CH<sub>4</sub>, and CO<sub>2</sub>) in the subtropical North Atlantic, *Atmos. Meas. Tech.*, 9, 2315–2333, <https://doi.org/10.5194/amt-9-2315-2016>, 2016.

García O. E., Schneider M., Ertl B., Sepúlveda E., Borger C., Diekmann C., Wiegeler A., Hase F., Barthlott S., Blumenstock T., Raffalski U., Gómez-Peláez A., Steinbacher M., Ries L., de Frutos A. M.: The MUSICA IASI CH<sub>4</sub> and N<sub>2</sub>O products and their comparison to HIPPO, GAW and NDACC FTIR references, *Atmos. Meas. Tech.*, 11, 4171–4215, <https://doi.org/10.5194/amt-11-4171-2018>, 2018.

Guedj S., Guidard V., Mahfouf J. F. : Preliminary studies towards the use of IASI PC products in the Météo-France global data assimilation system, 2015.

George M., Clerbaux C., Hurtmans D., Turquety S., Coheur P.-F., Pommier M., Hadji-Lazaro J., Edwards D. P., Worden H., Luo M., Rinsland C., and McMillan W.: Carbon monoxide distributions from the IASI/METOP mission: evaluation with other space-borne remote sensors, *Atmos. Chem. Phys.*, 9, 8317–8330, <https://doi.org/10.5194/acp-9-8317-2009>, 2009.

Goldberg M. D., Qu Y., McMillin L. M., Wolf W., Zhou L., Divakarla M.: AIRS near-real-time products and algorithms in support of operational numerical weather prediction, in *IEEE Transactions on Geoscience and Remote Sensing*, vol. 41, no. 2, pp. 379-389, Feb. 2003, doi: 10.1109/TGRS.2002.808307, 2003.



Goode J. G., Yokelson R. J., Ward D. E., Susott R. A., Babbitt R. E., Davies M. A., and Hao W. M.: Measurements of excess O<sub>3</sub>, CO<sub>2</sub>, CO, CH<sub>4</sub>, C<sub>2</sub>H<sub>4</sub>, C<sub>2</sub>H<sub>2</sub>, HCN, NO, NH<sub>3</sub>, HCOOH, CH<sub>3</sub>COOH, HCHO, and CH<sub>3</sub>OH in 1997 Alaskan biomass burning plumes by airborne Fourier transform infrared spectroscopy (AFTIR), *J. Geophys. Res.*, 105 (D17), 22147–22166, <https://doi.org/10.1029/2000JD900287>, 2000.

Gordon, L.S. Rothman I.E., Hill C., Kochanov R.V., Tan Y., Bernath P.F., Birk M., Boudon V., Campargue A., Chance K.V., Drouin B.J., Flaud J.-M., Gamache R.R., Hodges J.T., Jacquemart D., Perevalov V.I., Perrin A., Shine K.P., Smith M.-A.H., Tennyson J., Toon G.C., Tran H., Tyuterev V.G., Barbe A., Császár A.G., Devi V.M., Furtenbacher T., Harrison J.J., Hartmann J.-M., Jolly A., Johnson T.J., Karman T., Kleiner I., Kyuberis A.A., Loos J., Lyulin O.M., Massie S.T., Mikhailenko S.N., Moazzen-Ahmadi N., Müller H.S.P., Naumenko O.V., Nikitin A.V., Polyansky O.L., Rey M., Rotger M., Sharpe S.W., Sung K., Starikova E., Tashkun S.A., Vander Auwera J., Wagner G., Wilzewski J., Wcisło P., Yu S., Zak E.J.: The HITRAN2016 molecular spectroscopic database, *Journal of Quantitative Spectroscopy and Radiative Transfer*, Volume 203, 2017, Pages 3-69, ISSN 0022-4073, <https://doi.org/10.1016/j.jqsrt.2017.06.038>, 2017.

Gordon, I.E., Rothman, L.S., Hargreaves, R.J., Hashemi, R., Karlovets, E.V., Skinner, F.M., Conway, E.K., Hill, C., Kochanov, R.V., Tan, Y., Wcisło, P., Finenko, A.A., Nelson, K., Bernath, P.F., Birk, M., Boudon, V., Campargue, A., Chance, K.V., Coustenis, A., Drouin, B.J., Flaud, J. –M., Gamache, R.R., Hodges, J.T., Jacquemart, D., Mlawer, E.J., Nikitin, A.V., Perevalov, V.I., Rotger, M., Tennyson, J., Toon, G.C., Tran, H., Tyuterev, V.G., Adkins, E.M., Baker, A., Barbe, A., Canè, E., Császár, A.G., Dudaryonok, A., Egorov, O., Fleisher, A.J., Fleurbaey, H., Foltynowicz, A., Furtenbacher, T., Harrison, J.J., Hartmann, J. –M., Horneman, V. –M., Huang, X., Karman, T., Karns, J., Kassi, S., Kleiner, I., Kofman, V., Kwabia–Tchana, F., Lavrentieva, N.N., Lee, T.J., Long, D.A., Lukashchanskaya, A.A., Lyulin, O.M., Makhnev, V.Y., Matt, W., Massie, S.T., Melosso, M., Mikhailenko, S.N., Mondelain, D., Müller, H.S.P., Naumenko, O.V., Perrin, A., Polyansky, O.L., Raddaoui, E., Raston, P.L., Reed, Z.D., Rey, M., Richard, C., Tóbiás, R., Sadiq, I., Schwenke, D.W., Starikova, E., Sung, K., Tamassia, F., Tashkun, S.A., Auwera, J. Vander, Vasilenko, I.A., Vignati, A.A., Villanueva, G.L., Vispoel, B., Wagner, G., Yachmenev, A., Yurchenko, S.N. The HITRAN2020 molecular spectroscopic database. *J. Quant. Spectrosc. Radiat. Transf.* 277, 107949 (2022). doi:10.1016/j.jqsrt.2021.107949, 2022.

Hadji-Lazaro J. : Utilisation des réseaux de neurones pour l'inversion d'observations spatiales et la détermination des concentrations de constituants minoritaires dans la troposphère, 1 vol., 245 p., Thèse de doctorat Océanologie, météorologie et environnement Paris 6 1999, 1999PA066609, <http://www.theses.fr/1999PA066609>, 1999.

Hart M. A., Cooper N., Green D., Lipson M.: Urban Climate Science for Planning Healthy Cities, The Synergistic Impacts of Urban Air Pollution Compounding Our Climate Emergency, 978-3-03-087597-8, 978-3-03-087598-5, 10.1007/978-3-030-87598-5\_16, 2022.

IASI Level 1: Product Guide, EUM/OPS - EPS/MAN/04/ 0032 v5 e - signed, 6 September, 2019.



Karagulian F., Clarisse L., Clerbaux C., Prata A.J., Hurtmans D., Coheur P.-F.: Detection of volcanic SO<sub>2</sub>, ash, and H<sub>2</sub>SO<sub>4</sub> using the Infrared Atmospheric Sounding Interferometer (IASI). *J. Geophys. Res.*, 115, D00L02, DOI: 10.1029/2009JD012786, 2010.

Khaykin S., Legras B., Bucci S. et al.: The 2019/20 Australian wildfires generated a persistent smoke-charged vortex rising up to 35 km altitude. *Commun Earth Environ* 1, 22 (2020). <https://doi.org/10.1038/s43247-020-00022-5>, 2020.

Li Q. L., Jacob D. J., Bey I., Yantosca R. M., Zhao Y., Kondo Y., and Notholt J.: Atmospheric hydrogen cyanide (HCN): Biomass burning source, ocean sink? *Geophys. Res. Lett.*, 27, 357–360, 2000. <https://doi.org/10.1029/1999gl010935>, 2000.

Logan J. A., Prather M. J., Wofsy S. C., and McElroy M. B.: Tropospheric, chemistry: A global perspective, *J. Geophys. Res.*, 86, 7210–7254, 1981.

Mather T.A., Allen A.G., Davison B., Pyle D., Oppenheimer C., McGonigle A.J.S.: Nitric acid from volcanoes. *Earth and Planetary Science Letters*. 218. 17-30. 10.1016/S0012-821X(03)00640-X, 2004.

Matricardi M., A principal component based version of the RTTOV fast radiative transfer model. *Q.J.R. Meteorol. Soc.*, 136: 1823-1835. <https://doi.org/10.1002/qj.680>, 2010.

Matricardi M. and McNally A.P: The direct assimilation of principal components of IASI spectra in the ECMWF 4D-Var. *Q.J.R. Meteorol. Soc.*, 140: 573-582. <https://doi.org/10.1002/qj.2156>, 2014.

Millard G. A., Mather T. A., Pyle D. M., Rose W. I., Thornton B.: Halogen emissions from a small volcanic eruption: Modeling the peak concentrations, dispersion, and volcanically induced ozone loss in the stratosphere. *Geophys. Res. Lett.*, 33, Article number L19815, doi:10.1029/2006GL026959, 2006.

Moussallam Y., Tamburello G., Peters N., Apaza F., Schipper C. I., Curtis A., Aiuppa A., Masias P., Boichu M., Bauduin S., Barnie T., Bani Philipson, Giudice G., Moussallam M.: Volcanic gas emissions and degassing dynamics at Ubinas and Sabancaya volcanoes: implications for the volatile budget of the central volcanic zone. *Journal of Volcanology and Geothermal Research*, 343, p. 181-191. ISSN 0377-0273, 2017.

Razavi A., Karagulian F., Clarisse L., Hurtmans D., Coheur P.-F., et al.: Global distributions of methanol and formic acid retrieved for the first time from the IASI/MetOp thermal infrared sounder. *Atmospheric Chemistry and Physics*, European Geosciences Union, pp.857-872. 10.5194/acp-11-857-2011. hal-00516518, 2011.

Reath K., Pritchard M., Poland M., Delgado F., Carn S., Coppola D., et al. : Thermal, deformation, and degassing remote sensing time series (CE 2000–2017) at the 47 most active volcanoes in Latin America: Implications for volcanic systems. *Journal of Geophysical Research: Solid Earth*, 124, 195– 218. <https://doi.org/10.1029/2018JB016199>, 2019.

R'Honi Y., Clarisse L., Clerbaux C., Hurtmans D., Dufлот V., Turquety S., Ngadi Y., and Coheur P.-F.: Exceptional emissions of NH<sub>3</sub> and HCOOH in the 2010 Russian wildfires, *Atmos. Chem. Phys.*, 13, 4171–4181, <https://doi.org/10.5194/acp-13-4171-2013>, 2013.



Rosanka S., Franco B., Clarisse L., Coheur P.-F., Pozzer A., Wahner A., and Taraborrelli D.: The impact of organic pollutants from Indonesian peatland fires on the tropospheric and lower stratospheric composition, *Atmos. Chem. Phys.*, 21, 11257–11288, <https://doi.org/10.5194/acp-21-11257-2021>, 2021.

Rose W.I., Millard G.A., Mather T.A., Hunton D.E. Anderson B., Oppenheimer C., Thornton B.F., Gerlach T.M., Viggiano A.A., Kondo Y., Miller T.M., Ballenthin J.O.: Atmospheric chemistry of a 33–34 hour old volcanic cloud from Hekla Volcano (Iceland): Insights from direct sampling and the application of chemical box modeling. *J. Geophys. Res.* 111, article numberD20206, doi:10.1029/2005JD006872, 2006.

Sennert S.K. (ed.): Global Volcanism Program, 2015. Report on Calbuco (Chile), Weekly Volcanic Activity Report, 19 August–25 August 2015. Smithsonian Institution and US Geological Survey, 2015.

Sennert S.K. (ed.): Global Volcanism Program, 2019. Report on Raikoke (Russia). Weekly Volcanic Activity Report, 19 June–25 June 2019. Smithsonian Institution and US Geological Survey, 2019.

Sennert S.K. (ed.): Global Volcanism Program, 2019. Report on Ubinas (Peru). Weekly Volcanic Activity Report, 17 July–23 July 2019. Smithsonian Institution and US Geological Survey, 2019.

Sharpe, S. W., Johnson, T. J., Sams, R. L., Chu, P. M., Rhoderick, G. C., and Johnson, P. A.: "Gas-phase databases for quantitative infrared spectroscopy." *Applied Spectroscopy* 58: 1452–1461, 2004.

Tamburello G., Aiuppa A., McGonigle A. J. S., Allard P., Cannata A., Giudice G., Kantzas E. P., and Pering T. D.: Periodic volcanic degassing behavior: The Mount Etna example, *Geophys. Res. Lett.*, 40, 4818– 4822, doi:10.1002/grl.50924, 2013.

Turquety S., Hurtmans D., Hadji-Lazaro J., Coheur P.-F., Clerbaux C., Josset D., and Tsamalis C.: Tracking the emission and transport of pollution from wildfires using the IASI CO retrievals: analysis of the summer 2007 Greek fires, *Atmos. Chem. Phys.*, 9, 4897–4913, <https://doi.org/10.5194/acp-9-4897-2009>, 2009.

Van Damme M., Clarisse L., Heald C. L., Hurtmans D., Ngadi Y., Clerbaux C., Dolman A. J., Erismann J. W., and Coheur P. F.: Global distributions and trends of atmospheric ammonia (NH<sub>3</sub>) from IASI satellite observations, *Atmos. Chem. Phys. Discuss.*, 13, 24,301–24,342, doi:10.5194/acpd-13-24301-2013, 2013.

Van Damme M., Whitburn S., Clarisse L., Clerbaux C., Hurtmans D., and Coheur P.-F.: Version 2 of the IASI NH<sub>3</sub> neural network retrieval algorithm: near-real-time and reanalysed datasets, *Atmos. Meas. Tech.*, 10, 4905–4914, <https://doi.org/10.5194/amt-10-4905-2017>, 2017.

Van Damme M., Clarisse L., Franco F., Sutton M., Willem Erismann J. et al.: Global, regional and national trends of atmospheric ammonia derived from a decadal (2008–2018) satellite record. *Environmental Research Letters*, IOP Publishing, 2021, 16, pp.055017, doi:10.1088/1748-9326/abd5e0, 2021.

Varley N., Taran Y.: Degassing processes of Popocatepetl and Volcán de Colima, Mexico. *10.1144/GSL.SP.2003.213.01.16*, 2003.



Venzke E. (ed.): Report on Ubinas (Peru), Bulletin of the Global Volcanism Network, 44:9. Smithsonian Institution. <https://doi.org/10.5479/si.GVP.BGVN201909-354020>, Global Volcanism Program, 2019.

Wespes, C., Hurtmans, D., Chabrilat, S., Ronsmans, G., Clerbaux, C., and Coheur, P.-F.: Is the recovery of stratospheric O<sub>3</sub> speeding up in the Southern Hemisphere? An evaluation from the first IASI decadal record (2008–2017), Atmos. Chem. Phys., 19, 14031–14056, <https://doi.org/10.5194/acp-19-14031-2019>, 2019.

Wright C.J., Hindley N.P., Alexander M.J. et al. : Surface-to-space atmospheric waves from Hunga Tonga-Hunga Ha’apai eruption. Nature (2022). <https://doi.org/10.1038/s41586-022-05012-5>, 2022.

Zarzana J. K., Selimovic V., Koss A. R., Sekimoto K., Coggon M. M., Yuan B., Dubé W. P., Yokelson R. J., Warneke C., De Gouw J. A., Roberts J. M., and Brown S. S.: Primary emissions of glyoxal and methylglyoxal from laboratory measurements of open biomass burning Atmos. Chem. Phys., 18, 15451–15470, 2018, <https://doi.org/10.5194/acp-18-15451-2018>, 2018.